The Generic Nature of the Tropospheric Response to Sudden Stratospheric Warmings

IAN P. WHITE AND CHAIM I. GARFINKEL

The Hebrew University of Jerusalem, Institute of Earth Sciences, Edmond J. Safra Campus, Jerusalem, Israel

EDWIN P. GERBER

Courant Institute of Mathematical Sciences, New York University, New York, New York

MARTIN JUCKER

Climate Change Research Centre, University of New South Wales, Sydney, New South Wales, Australia

PETER HITCHCOCK

Department of Earth and Atmospheric Sciences, Cornell University, Ithaca, New York

JIAN RAO

The Hebrew University of Jerusalem, Institute of Earth Sciences, Edmond J. Safra Campus, Jerusalem, Israel

(Manuscript received 17 September 2019, in final form 19 December 2019)

ABSTRACT

The tropospheric response to midwinter sudden stratospheric warmings (SSWs) is examined using an idealized model. SSW events are triggered by imposing high-latitude stratospheric heating perturbations of varying magnitude for only a few days, spun off from a free-running control integration (CTRL). The evolution of the thermally triggered SSWs is then compared with naturally occurring SSWs identified in CTRL. By applying a heating perturbation, with no modification to the momentum budget, it is possible to isolate the tropospheric response directly attributable to a change in the stratospheric polar vortex, independent of any planetary wave momentum torques involved in the initiation of an SSW. Zonal-wind anomalies associated with the thermally triggered SSWs first propagate downward to the high-latitude troposphere after ~2 weeks, before migrating equatorward and stalling at midlatitudes, where they straddle the near-surface jet. After ~3 weeks, the circulation and eddy fluxes associated with thermally triggered SSWs evolve very similarly to SSWs in CTRL, despite the lack of initial planetary wave driving. This suggests that at longer lags, the tropospheric response to SSWs is generic and it is found to be linearly governed by the strength of the lower-stratospheric warming, whereas at shorter lags, the initial formation of the SSW potentially plays a large role in the downward coupling. In agreement with previous studies, synoptic waves are found to play a key role in the persistent tropospheric jet shift at long lags. Synoptic waves appear to respond to the enhanced midlatitude baroclinicity associated with the tropospheric jet shift, and preferentially propagate poleward in an apparent positive feedback with changes in the high-latitude refractive index.

---

1. Introduction

A change in the strength of the stratospheric polar vortex can have an appreciable influence on the position of the tropospheric midlatitude eddy-driven jet (e.g., Baldwin and Dunkerton 2001; Polvani and Kushner 2002; Kidston et al. 2015). In particular, there is considerable evidence in observations and models that a weakening of the polar vortex gives rise to a persistent

equatorward shift of the lower-tropospheric jet, whereas a strengthening of the vortex, such as that which occurs under ozone depletion, yields a poleward-shifted jet (e.g., Thompson and Solomon 2002). One of the most striking examples of this downward coupling occurs during a sudden stratospheric warming (SSW), wherein the polar vortex weakens and warms in the space of a few days (Scherhag 1952). Following an SSW, the equatorward tropospheric jet shift can persist for four or more weeks, substantially longer than the tropospheric decorrelation time scale in the absence of such an event (e.g., Baldwin and Dunkerton 2001; Gerber et al. 2010; Simpson et al. 2011). Extreme vortex events such as SSWs can thus provide a potential source of skill for extratropical weather forecasts on subseasonal to seasonal time scales (e.g., Sigmond et al. 2013).

It is implicit in a number of studies that the tropospheric response to SSWs can be separated into two approximate stages: 1) the mechanism by which the stratospheric anomalies are initially communicated downward to the troposphere, and 2) the subsequent amplification and persistence of the tropospheric jet shift (e.g., Song and Robinson 2004; Thompson et al. 2006). In terms of the former, the mechanisms are not well understood and many have been proposed, including "downward control" via the wave-induced zonally symmetric meridional circulation (Haynes et al. 1991; Thompson et al. 2006), a balanced nonlocal response to a stratospheric potential vorticity anomaly (Hartley et al. 1998; Ambaum and Hoskins 2002; Black and McDaniel 2004), as well as changes in planetary wave propagation, breaking and reflection either directly or indirectly in both the stratosphere and troposphere (e.g., Matsuno 1971; Chen and Robinson 1992; Perlwitz and Harnik 2003; Shaw et al. 2010; Hitchcock and Haynes 2016; Hitchcock and Simpson 2016; Smith and Scott 2016).

To explain the second stage (i.e., the persistent jet shift at longer lags), the general consensus is that synoptic wave feedbacks are necessary (Limpasuvan et al. 2004; Kushner and Polvani 2004; Song and Robinson 2004; Garfinkel et al. 2013; Hitchcock and Simpson 2014). Indeed, Domeisen et al. (2013) employed a dry dynamical core, to show that in the absence of synoptic wave feedbacks in the troposphere, the tropospheric response to an SSW would be a poleward-shifted jet, opposite to what is observed. To our knowledge, no study has explicitly tried to separate the short- and long-lag response. It is the latter upon which we focus in this study.

To understand how changes in stratospheric temperature (such as those found during an SSW) influence the troposphere, many studies have imposed temperature perturbations to the stratosphere (e.g., Williams 2006;

Lorenz and DeWeaver 2007). For instance, Polvani and Kushner (2002) and Kushner and Polvani (2004) developed a modification of the Held and Suarez (1994) forcing where tropospheric and stratospheric temperatures were relaxed to a chosen equilibrium state, to explore the impact of a high-latitude cooling on the troposphere. They demonstrated that the tropospheric response to a colder (stronger) polar vortex is a poleward-shifted jet stream. However, as they also relaxed the tropospheric temperatures, the downward impact was very sensitive to the details of the tropospheric climatology (e.g., Gerber and Polvani 2009). In fact, the magnitude of the tropospheric response to an identical stratospheric perturbation can differ by more than a factor of 3 depending on the tropospheric state (Garfinkel et al. 2013).

In another set of experiments, Haigh et al. (2005) and Simpson et al. (2009) imposed a steady stratospheric warming at high latitudes and found an equatorward tropospheric jet shift (although the main aim of their work was to understand the tropospheric response to tropical stratospheric warming). All of these studies found that changes in tropospheric eddy momentum fluxes and their feedbacks with the tropospheric circulation are crucial for the obtained response. Further, Simpson et al. (2009) found that the changes in the quasigeostrophic refractive index (Matsuno 1970) could explain the tropospheric eddy changes.

While many studies have imposed thermal perturbations to the stratosphere to explore changes in stratospheric variability (e.g., Taguchi et al. 2001; Jucker et al. 2013), the focus has been on the climatological (steady or seasonally evolving) modifications by applying the heating continuously. As SSWs are associated with a sudden onset of a high-latitude warming, we take a novel approach in this study by imposing a warming for only a few days to initiate an SSW, before switching it off and examining the coupled stratosphere–troposphere response. To do this, we perform a number of integrations with varying-magnitude heating profiles, using the Model of an Idealized Moist Atmosphere (MiMA; Jucker and Gerber 2017) and compare the evolution of the forced SSWs with SSWs taken from a free-running control integration. We also perform one additional experiment with an imposed high-latitude cooling in order to generalize the results to all extreme vortex events.

By triggering an SSW using a heating perturbation rather than by a modulation of the momentum budget, our experiments allow us to explicitly isolate the part of the downward influence that is attributable to changes in the polar vortex (e.g., subsequent changes in planetary and synoptic wave propagation in response to the

weakened vortex), as opposed to the downward influence that is associated with the preceding planetary wave activity that drives a naturally occurring SSW, or with tropospheric precursors (as found to be important by a number of studies, e.g., Black and McDaniel 2004; Nakagawa and Yamazaki 2006; Karpechko et al. 2017; White et al. 2019).

Indeed, Plumb and Semeniuk (2003) found that upward-propagating planetary waves emanating from the troposphere can drive wind anomalies at successively lower levels akin to that observed during SSWs. In this case the downward migration occurs as a passive response to upward-propagating waves, such that downward migration during SSWs does not necessarily indicate any stratospheric influence on the troposphere. We will show that the tropospheric response to SSWs at longer lags is somewhat generic, insomuch that the evolution during the thermally triggered SSWs and the free-running SSWs (i.e., those initiated by momentum torques) are almost indistinguishable. We conclude that the persistent equatorward shift of the tropospheric jet at longer lags is independent of the wave fluxes that force an SSW, and that there is a genuine downward propagation of anomalies from the stratosphere (e.g., Hitchcock and Haynes 2016).

Section 2 provides a description of our model and experiments. Section 3 presents the results of our study, comparing SSWs in a free-running control integration (which are necessarily forced by momentum torques) with those that are thermally triggered. Finally, in section 4, a summary and discussion is provided.

2. Model and experimental setup

In this study we utilize the recently developed Model of an Idealized Moist Atmosphere (referred to hereafter as MiMA; Jucker and Gerber 2017). The most important features of MiMA that distinguish it from dry dynamical cores used in the studies aforementioned are its explicit treatment of moisture and radiation. These two features are important for simulating a realistic stratosphere and hence for stratosphere–troposphere coupling, which is the focus of this study.

a. MiMA

MiMA is an intermediate complexity atmospheric model with a dynamical core that has a variety of other well-motivated physical processes. Following Frierson et al. (2006), it includes a representation of large-scale moisture transport, latent heat release, a mixed layer ocean, a subgrid-scale convection scheme (Betts 1986; Betts and Miller 1986), and a Monin–Obukhov

similarity boundary layer scheme. Also incorporated is a more realistic representation of radiation, namely the Rapid Radiative Transfer Model (RRTM) radiation scheme (Mlawer et al. 1997; Iacono et al. 2000), which replaces the gray radiation scheme of Frierson et al. (2006). The RRTM scheme allows for representation of the radiative impacts of both ozone and water vapor.

Neither a sponge layer nor Rayleigh damping scheme is utilized; instead, the gravity wave scheme of Alexander and Dunkerton (1999) is used to represent gravity wave momentum deposition, following Cohen et al. (2014). The gravity wave scheme is also modified to ensure that any gravity wave momentum fluxes that do reach close to the model lid are deposited in the top three layers so as to avoid possible sponge layer feedbacks and spurious meridional circulations associated with imposing heating perturbations (Shepherd et al. 1996; Shepherd and Shaw 2004). Full details regarding the model can be found in Jucker and Gerber (2017).

To generate a relatively realistic climatology (see Fig. S1 in the online supplemental material) on which our runs will be based, a number of parameters have been updated from the original version provided by Jucker and Gerber (2017). We follow Garfinkel et al. (2020), who modified the lower boundary conditions of the model to generate as realistic a stationary wave pattern as possible. There are differences between our study and theirs and these are documented in section 1 of the supplemental material, although these differences do not affect our results quantitatively. Another difference from Jucker and Gerber (2017) and Garfinkel et al. (2020) is the use of a monthly climatology zonal-mean input ozone file, taken from the preindustrial era CMIP5 forcing, as opposed to an annual-mean ozone input file. We note that this does not change the results qualitatively, although the SSW frequency is slightly higher using the latter. We refer readers to Garfinkel et al. (2020) for details on the exact model setup.

b. Experimental setup

A series of runs are performed at T42 horizontal resolution (2.8° × 2.8°) and with 40 vertical levels spanning from the surface to ~0.01 hPa (i.e., close to 70 km). We start by running the model freely for 50 years after discarding the first 10 years to allow the mixed layer ocean to reach an equilibrium state. This 50-yr control integration is herein referred to as the CTRL run.

In CTRL, 22 SSWs are found using the WMO criterion (McInturff 1978) that the zonal-mean zonal wind at 60°N and 10 hPa must reverse, along with the extra conditions that the SSW must occur during November–April, returning to westerly winds for at
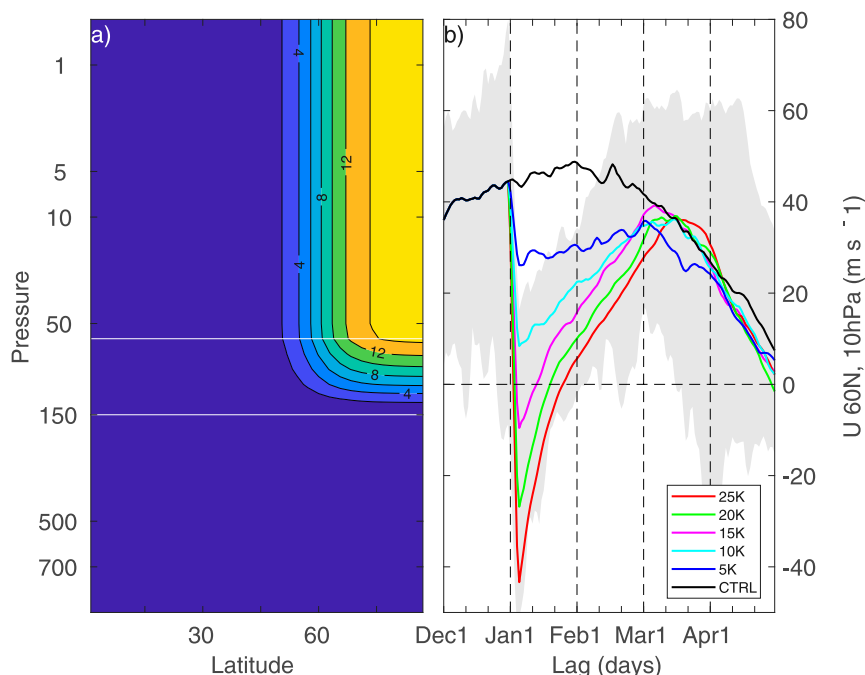
FIG. 1. (a) Idealized thermal-forcing profile with $Q = 15 \text{ K day}^{-1}$. The two horizontal lines indicate the region where the forcing linearly drops off between $p_t = 60 \text{ hPa}$ and $p_b = 150 \text{ hPa}$. All other parameters are as in section 2b. (b) Time series from 1 Dec to 1 May of the ensemble-mean $\bar{u}$ at 60°N, 10 hPa for each of the five PTRB experiments and CTRL. Gray shading shows the daily maximum and minimum $\bar{u}$ over all 15-K ensemble members.

least 10 consecutive days (to avoid counting final warmings), and that two consecutive SSW events must be separated by at least 20 consecutive days of westerly winds (following Charlton and Polvani 2007). The ratio of SSWs in CTRL is 0.44 yr^{-1}, which is a bit less than in observations (e.g., $\sim 0.65 \text{ yr}^{-1}$ in the latest ERA5 reanalysis). This may be due to the fact that in the climatology, the vortex is somewhat too strong and cold (by approximately $10–20 \text{ m s}^{-1}$ and $5–10 \text{ K}$, respectively; see Fig. S1a) compared to in observations.

Every 1 January in CTRL, we generate a branched integration where a *transient* warming in the extratropical stratosphere is imposed in order to trigger an SSW. We refer to these runs with imposed warming perturbations as PTRB experiments herein. For each PTRB, there are 50 ensemble members (from the 50 years in CTRL). To impose a warming, the following zonally symmetric term is added to the temperature tendency equation:

$$F(\varphi, p, t) = \tau(t)\Phi(\varphi)\Lambda(p), \qquad (1)$$

where

$$\tau(t) = \begin{cases} 1, & \text{if} \quad 0 < t - t_0 \leq N_d \ \text{days} \\ 0, & \text{otherwise} \end{cases}, \qquad (2)$$

$$\Phi(\varphi) = -\frac{Q}{2}\left[1 - \tanh\left(\frac{\varphi - \varphi_0}{\Delta\varphi}\right)\right], \qquad (3)$$

and

$$\Lambda(p) = \begin{cases} \dfrac{p - p_b}{p_t - p_b}, & \text{if} \quad p_t < p < p_b \\ 1, & \text{if} \quad p \leq p_t \\ 0, & \text{if} \quad p > p_b \end{cases}, \qquad (4)$$

and where t is the model time, t_0 is the reference time (midnight on 31 December), N_d is the prescribed duration of the heating, φ, φ_0, and $\Delta\varphi$ are the latitude, reference latitude at which the warming reaches half of its full magnitude and the width of the warming, respectively, Q is the heating rate per day (K day^{-1}), and p is the pressure level. The reference latitude and width are taken to be $\varphi_0 = 60°\text{N}$ and $\Delta\varphi = 5°$, respectively. To avoid sharp transitions in the vertical, the heating perturbation decreases linearly between p_t and p_b, which we choose to be $p_t = 60 \text{ hPa}$ and $p_b = 150 \text{ hPa}$ so as to limit the heating to the stratosphere and to avoid minimal interference with the troposphere below. An example heating profile with $Q = 15 \text{ K day}^{-1}$ is shown in Fig. 1a. Note that the stratospheric warming is applied to sigma

levels rather than pressure levels; however, the difference between the two is relatively small and hence does not affect our results quantitatively.

In total, five PTRB warming experiments are presented here, along with one PTRB cooling experiment, each with 50 ensemble members and with varying magnitude warmings and $N_d = 3$ days; the maximum thermal forcing is $Q = 25 \, \text{K day}^{-1}$, incrementally decreasing by 5 K down to $Q = 5 \, \text{K day}^{-1}$. The PTRB cooling experiment has a thermal forcing of $Q = -10 \, \text{K day}^{-1}$. For example, in the 15-K PTRB, a forcing of $Q = 15 \, \text{K day}^{-1}$ is switched on for 3 days, after which it is switched off and subsequently the model is allowed to run freely. Figure 1b shows the change in vortex strength (i.e., the ensemble mean zonal-mean zonal wind $\overline{u}$ at 60°N and 10 hPa) for each of the five PTRB warming experiments (colored lines) as well as the free-running CTRL (black line). By construction, the PTRB experiments follow CTRL throughout December until 1 January when the heating perturbation is switched on. The PTRB experiments then show a sudden weakening of the vortex followed by a slow recovery in the ensemble mean [although there is considerable spread among individual ensemble members as shown by the 15-K PTRB (gray shading)]. The magnitude of the weakening of $\overline{u}$ increases with increasing thermal forcing, with the 5- and 10-K PTRBs only weakening the vortex but with no reversal, whereas the 15-, 20-, and 25-K PTRBs all show a reversal in the ensemble mean. Over the next 2–3 months, $\overline{u}$ recovers to a state that is close to that found in CTRL in March–April.

Note that PTRB experiments where the duration of the thermal forcing has been varied have also been conducted (with $N_d = 5$ and 10 days). The key difference at longer lags is that the tropospheric response lasts for longer in conjunction with the thermal forcing duration. At shorter lags, a forcing that is imposed for longer, drives a stronger tropospheric response directly associated with the forcing itself that also lasts for a longer period (see the anomalous tropospheric westerlies in the bottom row of Fig. 2b). Hence, to avoid such direct tropospheric impacts that are not typical of observed SSWs, we limit the thermal forcing to $N_d = 3$ days.

Experiments have also been conducted wherein the vertical extent of the heating is modified. In particular, imposing the forcing only above $p_b = 70$ hPa still yielded a clear near-surface response (~30% weaker in magnitude), whereas restricting the heating to above $p_b = 30$ hPa, gave a much weaker near-surface response (along with a less barotropic structure). These results are in general agreement with Butler et al. (2010) insomuch that raising the lowest level of forcing does

influence the magnitude of the near-surface response, although the details are different as their forcing was substantially weaker. We further note that the results presented herein are insensitive to different horizontal and vertical resolutions (T85 horizontal and using 60 levels rather than 40).

The initial stratospheric and tropospheric states for each ensemble member are not the same and are essentially random. This is indicated by the spread of the individual ensemble members for the 15-K PTRB (gray shading) before 1 January in Fig. 1b. Hence, any signal in the PTRB anomaly composites in relation to CTRL represents the deterministic response to the thermally forced stratospheric anomalies, which are thus independent of the initial stratospheric and tropospheric states. Also, note that there are two years in CTRL for which $\overline{u}$ at 60°N and 10 hPa is negative on 30 December (and two others when $\overline{u}$ is less than $15 \, \text{m s}^{-1}$), and hence there is already a naturally occurring SSW even before a heating is imposed. Nevertheless, omitting these 2–4 years in our PTRB experiments does not change the results quantitatively.

3. Results: Zonal-mean circulation and wave evolution during free-running and thermally forced SSWs

We compare the evolution of the zonal-mean circulation and wave propagation/forcing between the 22 SSWs identified in CTRL (hereafter CTRL SSWs) and the thermally forced SSWs in PTRB. We focus primarily on the 15-K PTRB experiment although note that both the 10- and 15-K PTRB experiments provide similar results that are most similar to the CTRL SSWs. Nevertheless, we also make interexperiment comparisons to examine the tropospheric response sensitivity to the various magnitude thermal forcings.

The anomalies in this section are all deviations away from the unfiltered daily climatology in CTRL. For example, anomalies averaged over lags 1–3 in PTRB are calculated as the deviations away from the daily climatology in CTRL averaged over 1–3 January. By construction therefore, in PTRB, the ensemble-mean anomalies are identically zero.

a. Zonal wind, NAM, and temperature evolution

Composites of zonal-mean zonal wind $\overline{u}$ (black contours) and zonal-mean temperature $\overline{T}$ (shading) are shown in Fig. 2 for different lag stages during the life cycle of the CTRL SSWs (top row) and during the PTRB SSWs (bottom row). Prior to the onset (Fig. 2a), the CTRL SSWs are marked by both stratospheric and tropospheric precursors. In particular, there is a weaker and warmer polar vortex with largest magnitudes above
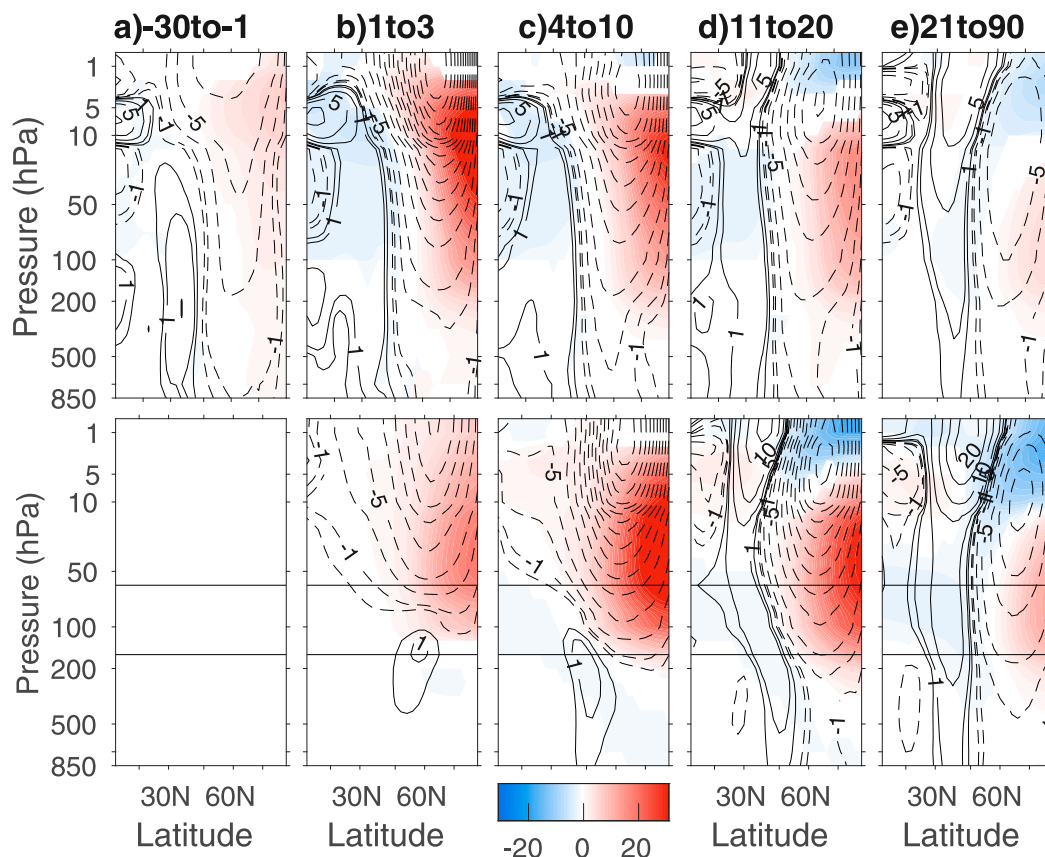
FIG. 2. (top) Latitude–height cross sections of the $\overline{T}$ (shading; K) and $\overline{u}$ (green contours; m s^{-1}) ensemble-mean SSW anomalies averaged over different lag stages in CTRL. Note that only $\overline{T}$ anomalies that are statistically significantly different from the climatology in CTRL are shaded. Solid (dashed) black contours represent positive (negative) $\overline{u}$ anomalies with contours at $\pm0.5, 1, 2.5, 5, 10, \ldots$ m s^{-1}. (bottom) As in the top row, but for the 15-K PTRB experiment. Note that the lags for the PTRB experiments are according to the start of the thermal forcing stage (1 Jan). Thin horizontal lines are as in Fig. 1a.

~50 hPa. There is also evidence of tropospheric pre-conditioning with $\overline{u} < 0$ anomalies at high latitudes and $\overline{u} > 0$ south of ~50°N. Such precursors have been found in observations (e.g., Black and McDaniel 2004; Cohen and Jones 2011; Garfinkel et al. 2010) although their representation in models are generally model dependent (Gerber et al. 2010). The vertical tripole of tropical wind anomalies represent the winds of the quasi-biennial oscillation, and in particular, with easter-lies in the lower-middle stratosphere, provide favorable conditions for SSWs to occur (Holton and Tan 1980). By construction, there are no ensemble-mean anomalies in PTRB prior to the onset date (Fig. 2a, bottom).

Lags 1–3 (Fig. 2b) represent the early onset in CTRL SSWs and the forcing stage in PTRB SSWs. In CTRL, there is a clear intensification of the $\overline{u} < 0$ and $\overline{T} > 0$ anomalies in the stratosphere. In PTRB, the $\overline{T} > 0$ anomalies are located above 100 hPa by construction, and via thermal wind balance, give rise to a weakened

polar vortex. Below ~100 hPa, weak-valued $\overline{u} > 0$ anomalies centered on 60°N develop (although in-significant). These tropospheric $\overline{u}$ anomalies develop as a direct response to the heating perturbation aloft. In particular, in the region of heating, upwelling occurs, with corresponding downwelling at lower latitudes. To close the induced circulation, there is poleward motion below and equatorward motion aloft (not shown). The anomalous $\overline{u} > 0$ near 150 hPa, 60°N forms due to the Coriolis influence on the anomalous poleward motion.

As the lags progress, the development of the strato-spheric anomalies in both CTRL and PTRB are rather similar. There is a poleward and downward movement of the $\overline{u}$ and $\overline{T}$ anomalies, with the $\overline{T}$ anomalies stalling in the lower stratosphere where they persist for up to three months (in agreement with the circulation devel-opment during polar-night jet oscillation events; Kuroda and Kodera 2001; Hitchcock et al. 2013). A recovery of the vortex starts in the upper stratosphere after 1–2 weeks
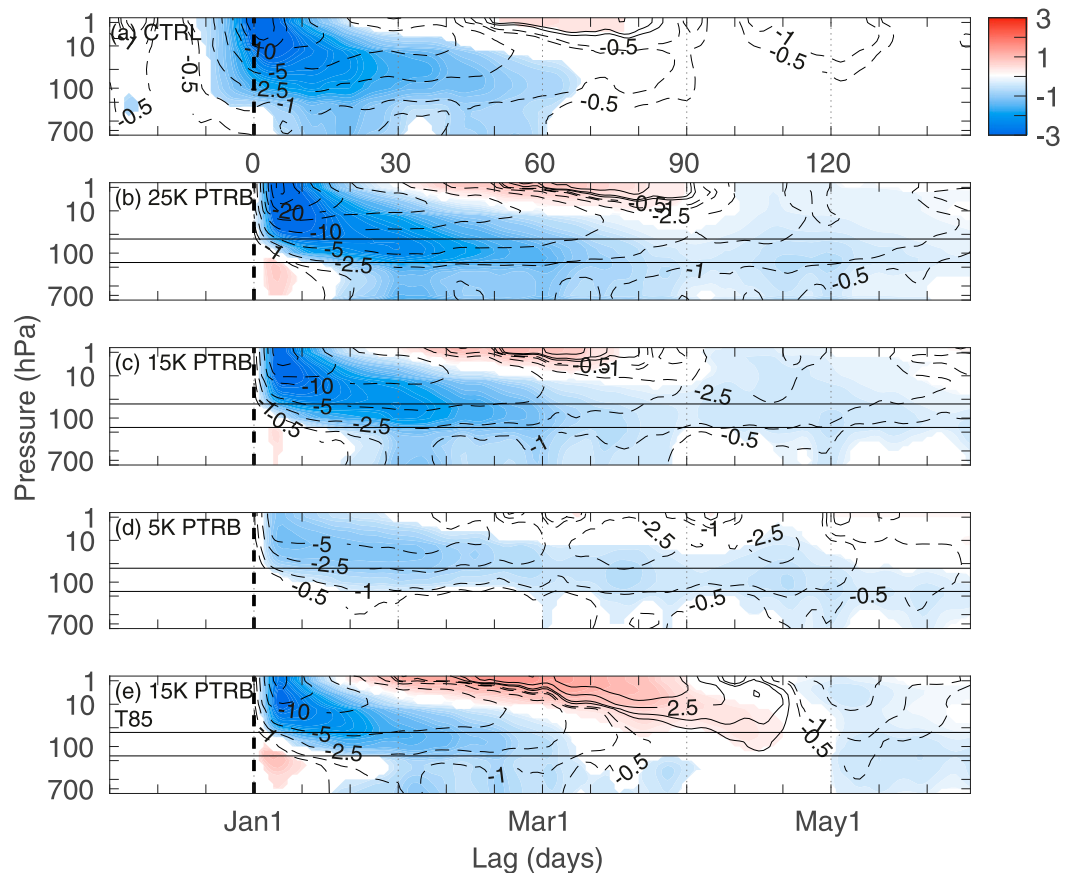
FIG. 3. Height–lag composites of the NAM index (shading with units of standard deviations) averaged over 60°–87°N and over all SSWs in the (a) CTRL run, (b) 25-K, (c) 15-K, (d) 5-K, and (e) T85 15-K PTRB experiments. Note that only the NAM index that is statistically significant at the 95% level is shaded. The black contours show $\overline{u}$ anomalies averaged over 60°–80°N with the same contour spacing as in Fig. 2. Thick dashed black vertical lines indicate the SSW onset in (a) and 1 Jan in (b)–(d), and the thin dashed black lines indicate every 30 days thereafter.

due to the suppression of upward-propagating waves (see later figures). The tropical easterly anomalies at all lags are likely related to the weakened Brewer–Dobson circulation (see later Fig. 10), which drives easterlies via Coriolis torques, and show up in the meridional circulation anomalies associated with the annular mode (e.g., Thompson and Wallace 2000).

In the troposphere, the $\overline{u}$ anomalies are somewhat different between CTRL and PTRB, with the former showing an intensification of the preexisting tropospheric precursors and an equatorward shift by ~5°. In PTRB, however, there is a downward propagation of the stratospheric $\overline{u} < 0$ anomalies into the troposphere, beginning at lags 11–20. In particular, the tropospheric $\overline{u} > 0$ anomalies found during the forcing stage (Fig. 2b) migrate equatorward and are replaced by high-latitude $\overline{u} < 0$ anomalies that occur as an extension of the negative $\overline{u}$ anomalies associated with the weakened polar vortex. Together, these anomalies yield a tropospheric dipole akin to that found during CTRL SSWs, although

note that this dipole is initially located farther poleward at lags up until lag ~20.

To further highlight the downward propagation to the troposphere, Fig. 3 shows height–time composites of the northern annular mode (NAM) index (shading) and $\overline{u}$ anomalies (contours) for the CTRL SSWs (Fig 3a) and for various PTRB experiments (Figs. 3b–e). The NAM index is calculated as the area-averaged geopotential height anomalies north of 60°N, normalized by the standard deviation at each pressure level and multiplied by −1, as suggested by Baldwin and Thompson (2009), and $\overline{u}$ is averaged over 60°–80°N. Prior to the onset, there are no anomalies by construction in all PTRB experiments, whereas there is evidence of the precursors present in Fig. 2a in CTRL (top). Overall, the NAM index associated with the CTRL SSWs is similar in terms of magnitude and duration to observed SSWs (e.g., Karpechko et al. 2017).

After the onset, the general structure of the stratospheric anomalies is similar between CTRL and PTRB

with a sudden enhancement of negative NAM anomalies close to the onset date followed by recovery first aloft, and persistence in the lower stratosphere. However, the PTRB experiments in Figs. 3b–d have NAM anomalies that persist for much longer than in CTRL. In particular, the anomalies associated with the PTRB SSWs last until ~90 days after the switch-on forcing (i.e., up to 1 April) whereas in CTRL they last for ~65–70 days in the lower stratosphere. The second negative-NAM anomaly peak in April–May is associated with an earlier onset of the date of the final warming in all PTRB runs. In CTRL, the average final warming date over all 50 years is 12 May, whereas in PTRB, the average final warming date ranges from 28 April to 6 May.

The NAM index for our T85 15-K PTRB run (Fig. 3e) appears to explain the more persistent NAM in our T42 PTRB runs compared to in CTRL. The NAM in T85 persists for a similar period to the CTRL SSWs (although note the stronger recovery in T85 compared to in T42). Previous studies have found that coarser-resolution models tend to have more persistent annular mode variability (e.g., Gerber et al. 2008) and comparison of Figs. 3c and 3e confirm this in MiMA. Nevertheless, our T42 and T85 runs are qualitatively similar and the essential dynamics at play are the same (not shown). Further, the fluctuation dissipation theorem (Leith 1975) indicates that the extratropical jet response can be overly sensitive to external forcing if the intrinsic annular-mode time scales are too long, but a comparison of Figs. 3a and 3c (as well as Fig. 5 below) suggests that the PTRB and CTRL have tropospheric responses of similar magnitude and hence the response to external forcing is not exaggerated in our experiments.

In terms of the downward influence on the troposphere, the CTRL SSWs, 25- and 15-K PTRB experiments exhibit the classical "dripping-paint" pattern found by Baldwin and Dunkerton (2001). This is in contrast to the 5-K PTRB experiment that does not show any statistically significant downward propagation below ~200 hPa aside from a weakly negative tropospheric NAM in March. In particular, in the 15- and 25-K PTRB, the NAM and $\overline{u}$ anomalies gradually propagate down to ~300–400 hPa over the first ~15–20 days, which is then followed by a sudden, barotropic response down to the surface. Further, the 25-K PTRB shows evidence of the largest-magnitude and most persistent tropospheric response. Note that the positive tropospheric NAM in the 25- and 15-K PTRBs at early lags represents the anomalous tropospheric westerlies found in Fig. 2 at lags close to the forcing.

In observations, the tropospheric $\overline{u}$ anomalies following an SSW event project onto the leading mode of variability [i.e., the first empirical orthogonal function (EOF) of zonal wind] (e.g., Simpson et al. 2011), which represents latitudinal shifts in the near-surface zonal-mean tropospheric jet. To this end, we present $\overline{u}$ anomalies at 850 hPa for the CTRL SSWs as well as the projection of these anomalies onto the first and second EOFs of $\overline{u}$ (hereafter referred to as EOF1 and EOF2, respectively) in Figs. 4a–c. Figures 4d–f shows the same except for the 15-K PTRB experiment. To calculate the EOFs, daily data for December–May are used, multiplied by $\sqrt{\cos\varphi}$ over 1°–87°N. It is clear that EOF1 represents latitudinal shifts in the climatological near-surface winds whereas EOF2 gives rise to a pulsing or broadening of the jet as expected (see black contours in Figs. 4d–f and horizontal line in Figs. 4a–c).

For the CTRL SSWs (Fig. 4, left), a dipole in $\overline{u}$ exists with negative (positive) anomalies straddling the December–February climatological jet core (horizontal line) at both negative and positive lags. The dipole at negative lags again indicates the tropospheric precursors seen in previous figures, although the $\overline{u}$ anomalies have larger magnitudes after the onset. It is clear from Figs. 4b and 4c that the near-surface response to SSWs mostly projects onto EOF1, with a much smaller projection onto EOF2. However, we note that the projection onto EOF2 does become more pronounced after lag ~30 compared to at earlier lags.

For the 15-K PTRB experiment (Fig. 4, right), the $\overline{u}$ anomalies project onto both EOF1 and EOF2. In agreement with Fig. 2, the $\overline{u} > 0$ anomalies initially start at higher latitudes before migrating equatorward and stalling at ~45°N after about 20 days (and also becoming significant). The significant negative anomalies at higher latitudes begin after ~10 days, in agreement with the ~10-day delay in the tropospheric response found in observations by Baldwin and Dunkerton (1999). Note that this 10-day delay does not appear in the CTRL SSWs likely due to the presence of tropospheric precursors. Looking more closely, the projection onto EOF2 precedes the projection onto EOF1 by ~5–10 days. This points to the equatorward shift of the anomalies as the lags progress. After ~20 days, $\overline{u}$ projects onto both EOFs, although with a bias toward EOF1 (cf. magnitudes of Figs. 4e,f). This structure is somewhat reminiscent of that during final warmings in agreement with Black et al. (2006) and Sheshadri et al. (2017), who found that the tropospheric response during final warmings is to project onto both EOF1 and EOF2. Nevertheless, we note the similarity between CTRL and PTRB at lags ≳30 where the projection onto EOF2 in CTRL becomes more pronounced.

A natural question arising from Figs. 2–4 is how the strength of the initial stratospheric warming relates to the subsequent strength and persistence of the
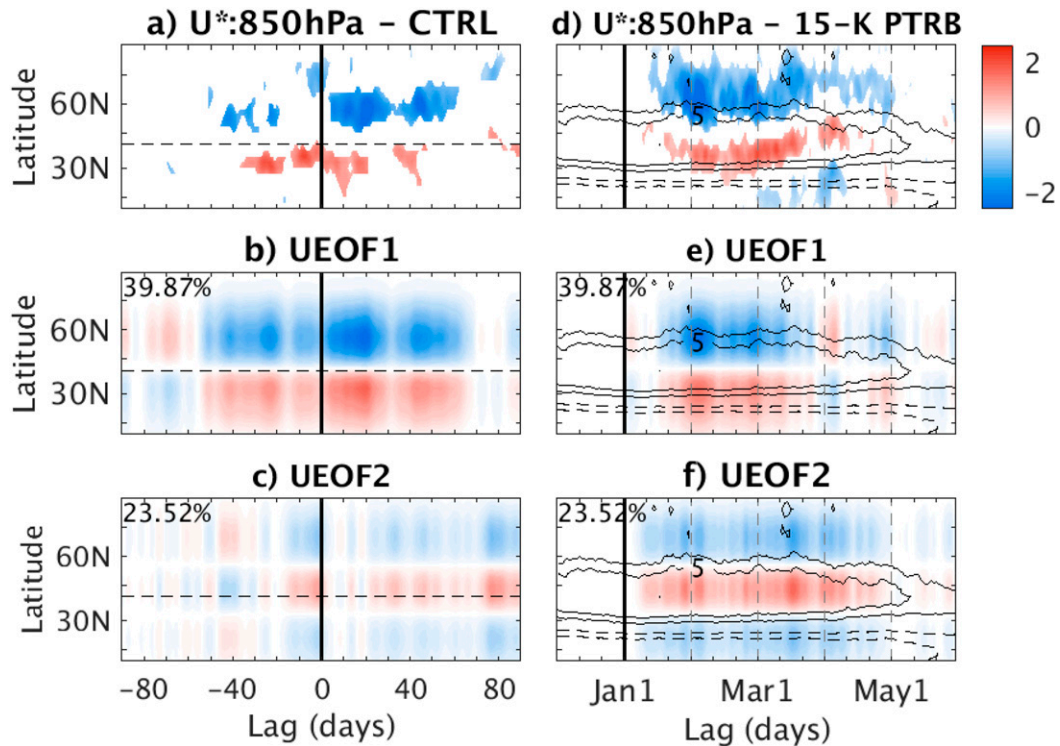
FIG. 4. (top) Latitude–lag composites of $\overline{u}$ anomalies at 850 hPa for the (a) CTRL SSWs and (d) 15-K PTRB SSWs. Note that only $\overline{u}$ anomalies that are statistically significant at the 95% level are shaded. (b),(e) Projection of $\overline{u}$ anomalies from the top row onto the first EOF of the CTRL run. The horizontal line indicates the December–February climatological $\overline{u}$ in CTRL. (c),(f) As in (b) and (e), but as a projection onto the second EOF. Black contours in (d)–(f) indicate the daily climatological $\overline{u}$ at this level with values at $\pm 2.5, 5, 10, \ldots \mathrm{m\,s}^{-1}$. Vertical lines indicate every 30 days.

tropospheric response. Hence, in Fig. 5a, the variability of the strength of the tropospheric response for all ensemble members for all PTRB experiments is shown as a scatterplot of the lower-stratospheric (100 hPa) $\overline{u}$ averaged over lags 11–90, plotted against $\overline{u}$ at 850 hPa averaged over lags 11–90. Figure 5b then addresses how the persistence of the tropospheric NAM varies in response to the stratospheric anomalies as a scatterplot of the 100-hPa NAM averaged over lags 11–90, against the percentage of days post onset that the NAM at 850 hPa is less than −1 standard deviation. Note that the PTRB cooling experiment is not included in Fig. 5b. Lag averages starting at lag 11 are used to limit the influence of the imposed forcing on the results. Nevertheless, the results are not sensitive to changes in the averaging lags, latitudes or pressure levels chosen, or to the NAM threshold used in Fig 5b.

Overall, it is clear that the PTRB heating experiments give rise to an equatorward-shifted near-surface jet, whereas the PTRB cooling gives rise to a poleward-shifted jet (with the exception of a few ensemble members). There is a clear linear relationship, with a more negative lower-stratospheric $\overline{u}$ anomaly and

NAM index resulting in a more negative near-surface $\overline{u}$ anomaly (Fig. 5a; $r = 0.93$) and persistent negative NAM (Fig. 5b; $r = -0.74$). There is some scatter among different experiments (particularly in Fig. 5b), indicative of the fact that the vortex state prior to the thermal forcing being initialized was already highly variable with some runs having an anomalously weak or strong vortex.

The regression slopes (shown at the top right in Figs. 5a,b) allow us to approximately quantify the magnitude of the downward impact. For instance, the near-surface $\overline{u}$ response to an SSW is ~30% of the strength of the lower-stratospheric $\overline{u}$ anomaly averaged over positive lags. Further, an averaged lower-stratospheric negative NAM of one standard deviation, leads to ~25%–30% of the following 90 days having a near-surface NAM of < -1 standard deviation. Note that using 10-hPa $\overline{u}$ anomalies on the abscissa in Fig. 5a, still yields a high correlation ($r = 0.82$) likely due to the imposed heating. If just the 22 CTRL SSWs are utilized in the calculation in Fig. 5a, then the correlations become $r = 0.83$ at 100 hPa and $r = 0.43$ at 10 hPa. Finally, the regression slopes for all variability in CTRL
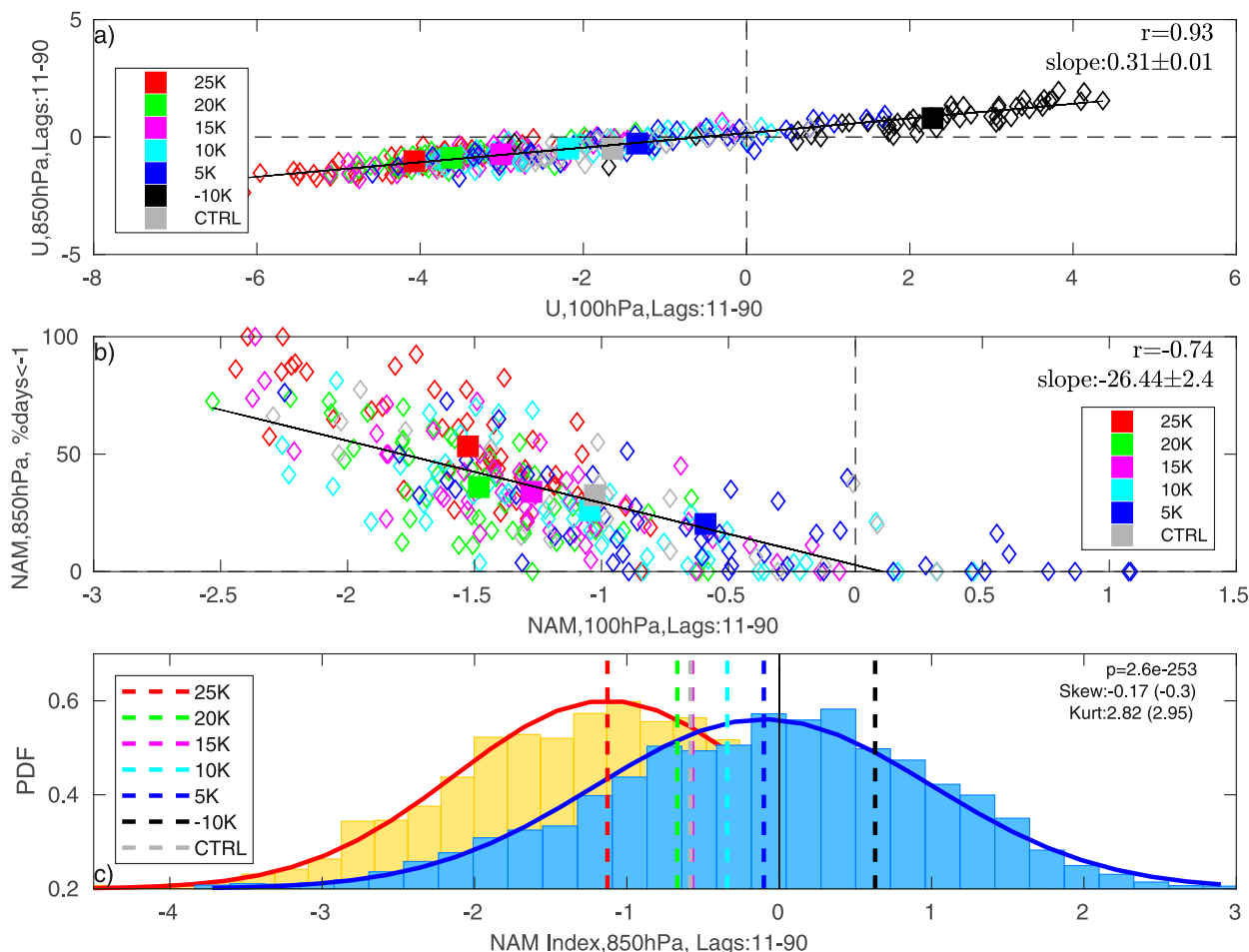
FIG. 5. (a) Scatterplot of $\overline{u}$ at 100 hPa against $\overline{u}$ at 850 hPa, both averaged over 60°–87°N and lags 11–90, for different PTRB experiments (see legend) and CTRL. Filled colored squares indicate the corresponding ensemble means for each experiment. (b) Scatterplot of the NAM index at 100 hPa averaged over lags 11–90, against the percentage of days post onset that the NAM at 850 hPa is smaller than a threshold of one standard deviation. Black lines show the line of best fit calculated using a least squares fit. The slope of the linear regression lines (along with the confidence intervals) and the correlation coefficients (r) are included at the top right of both (a) and (b). Note that the regression slopes are listed separately for CTRL and PTRB SSWs if they are significantly different from one another. (c) Histograms of the daily NAM index at 850 hPa for positive lags for the 25-K PTRB (orange/red) and the 5-K PTRB (blue). The Kolgomorov–Smirnov test is used to test the significance between the two histograms with the p value shown in the top right corner of (c). Also shown in the top right are the skewness and kurtosis for the two histograms with the 5-K PTRB values in parentheses. Colored dashed vertical lines represent the ensemble means for each PTRB experiment as well as for CTRL.

(calculated as monthly mean anomalies) is 0.45, which is perhaps surprisingly higher than the slope for just SSW variability as shown in Fig. 5a.

To further show that a stronger thermal perturbation yields a more-negative tropospheric NAM response, Fig. 5c shows histograms of the 850-hPa daily NAM indices at positive lags for the 25- and 5-K PTRB experiments (colored vertical lines indicate the ensemble means for the other three PTRB heating experiments, the PTRB cooling, and for CTRL). The main feature is that the 25-K PTRB leads to an overall shift of the tropospheric NAM toward more negative values in comparison to the 5-K PTRB rather than

there being large changes in the skewness or kurtosis of the respective histograms (see values in top right). This is in agreement with Simpson et al. (2011), Sigmond et al. (2013), and Hitchcock and Simpson (2014) who also found that the main stratospheric influence during SSWs is to bias the troposphere to a more negative NAM-like state. We note that the 15-K PTRB produces a near-surface response of very similar magnitude to in CTRL (cf. pink and gray vertical lines).

In summary, the evolution of $\overline{u}$ and $\overline{T}$ in the CTRL SSWs and the thermally triggered SSWs become very similar after ~2–3 weeks. Prior to that, the thermally

triggered SSWs show a gradual poleward and downward migration of $\overline{u} < 0$ from the lower stratosphere to the near-surface at high latitudes, where they then migrate equatorward and stall at midlatitudes, projecting predominantly onto EOF1, and with a smaller projection onto EOF2. It appears that the strength of the tropospheric response to SSWs mostly depends on the magnitude of the heating perturbation in the lower stratosphere and acts to bias the tropospheric NAM to a more negative state.

Herein, the lag stages 4–10 and 11–20 are averaged into one (4–20). This is because the aim of this paper is to examine the long-lag (i.e., $\gtrsim 3$ week) tropospheric response to SSWs. The mechanisms behind the initial downward impact (i.e., the short-lag response), are beyond the scope of this paper.

b. Planetary and synoptic wave evolution

In this section we examine the wave evolution during SSWs in both the CTRL and PTRB experiments. In particular, we plot the Eliassen–Palm (EP) flux $\mathbf{F} = (F^{(\varphi)}, F^{(z)})$, where

$$F^{(\varphi)} = a\rho_0 \cos\varphi \left(\overline{u}_z \frac{\overline{v'\theta'}}{\overline{\theta}_z} - \overline{u'v'} \right) \quad \text{and} \quad (5a)$$

$$F^{(z)} = a\rho_0 \cos\varphi \left\{ \left[f - \frac{(\overline{u}\cos\varphi)_\varphi}{a\cos\varphi} \right] \frac{\overline{v'\theta'}}{\overline{\theta}_z} \right\} \quad (5b)$$

are the meridional and vertical components of the EP flux in spherical coordinates. In these equations, z is the log-pressure height, v and w are the meridional and vertical components of the wind, θ is the potential temperature, and a, f, and ρ_0 are Earth's radius, Coriolis parameter, and background density profile, respectively. Overbars and primes represent zonal averages and the deviations therefrom, respectively. The divergence of $\mathbf{F}$:

$$\Pi \equiv \frac{\nabla \cdot \mathbf{F}}{\rho_0 a \cos\varphi} \quad (6)$$

$$= \frac{1}{\rho_0 a \cos\varphi} \left[\frac{1}{a\cos\varphi} \frac{\partial}{\partial\varphi} (F^{(\varphi)} \cos\varphi) + \frac{\partial F^{(z)}}{\partial z} \right],$$

in the zonal-mean zonal momentum budget:

$$\frac{\partial \overline{u}}{\partial t} + \overline{v}^* \left[\frac{(\overline{u}\cos\varphi)_\varphi}{a\cos\varphi} - f \right] + \overline{w}^* \frac{\partial \overline{u}}{\partial z} = \frac{\nabla \cdot \mathbf{F}}{\rho_0 a \cos\varphi} + \overline{X}, \quad (7)$$

represents the wave forcing of $\overline{u}$ (Andrews et al. 1987), and $(\overline{v}^*, \overline{w}^*)$ and $\overline{X}$ represent the meridional and vertical components of the residual mean meridional

circulation (see section 3d) and nonconservative effects/parameterized gravity wave drag, respectively. Hence, a convergence of wave activity ($\nabla \cdot \mathbf{F} < 0$) acts to weaken $\overline{u}$ and and vice versa, although on longer time scales, the main balance in Eq. (7) is between Π and the $\overline{v}^*$ term in brackets. In particular, $\nabla \cdot \mathbf{F} < 0$ is balanced by a poleward residual circulation $f\overline{v}^* > 0$, and vice versa (e.g., Martineau et al. 2018). The wavenumber contributions to $\mathbf{F}$ and Π can be quantified by first filtering u, v, w, and θ using a Fourier transform. Note that in this section, and in all subsequent figures that involve eddy contributions, the lowest level of the plots are cut off at 700 hPa. This is to avoid issues with topography when decomposing variables into different wavenumbers.

Figure 6 shows latitude–height composites of the EP flux divergence term $\Pi = \nabla \cdot \mathbf{F}/\rho_0 a\cos\varphi$ (shading), EP fluxes $\mathbf{F}$ (arrows), and $\overline{u}$ (contours; as in Fig. 2) anomalies for the CTRL SSWs at various lag stages. The $\mathbf{F}$ term is split into planetary wave (zonal wavenumbers 1–3; top) and synoptic wave (wavenumbers 4+; bottom) contributions. Note that $\mathbf{F}$ is plotted only if $F^{(\varphi)}$ or $F^{(z)}$ is significantly different from the climatology. Prior to lag zero (Fig. 6a), the weaker vortex is driven by an enhanced convergence of upward-propagating planetary wave anomalies throughout the high-latitude stratosphere. There is also convergence in the troposphere north of 45°N that appears to contribute to the precursory equatorward jet shift. At lags 1–3 (Fig. 6b), there is continued convergence of planetary waves inside the polar vortex as well as at 45°N in the mid- to lower troposphere, along with anomalous $\Pi > 0$ in the high-latitude upper troposphere. In the midlatitude stratosphere, the anomalous synoptic-wave convergence may result from breaking planetary waves that generate smaller-scale features.

At lags 4+ (Figs. 6c, d) planetary wave $\mathbf{F}$ anomalies are generally oriented poleward and downward along with anomalous $\Pi > 0$ in the high-latitude stratosphere, although the magnitudes of $\mathbf{F}$ and Π for planetary waves decrease at lags 21–90. This suppression following an SSW is the expected response to the weakened polar vortex (e.g., Limpasuvan et al. 2004). The presence of tropospheric precursors makes it difficult to separate the anomalies that are associated with the downward propagation from the preexisting tropospheric anomalies. The region of anomalous planetary wave $\Pi < 0$ near 55°–60°N in the middle troposphere contributes to the maintenance of the negative high-latitude $\overline{u}$ anomalies.

Tropospheric poleward-propagating synoptic waves are present at all lags straddling the $\overline{u}$ dipole. In particular, they likely are very important in maintaining the persistent tropospheric jet shift via equatorward
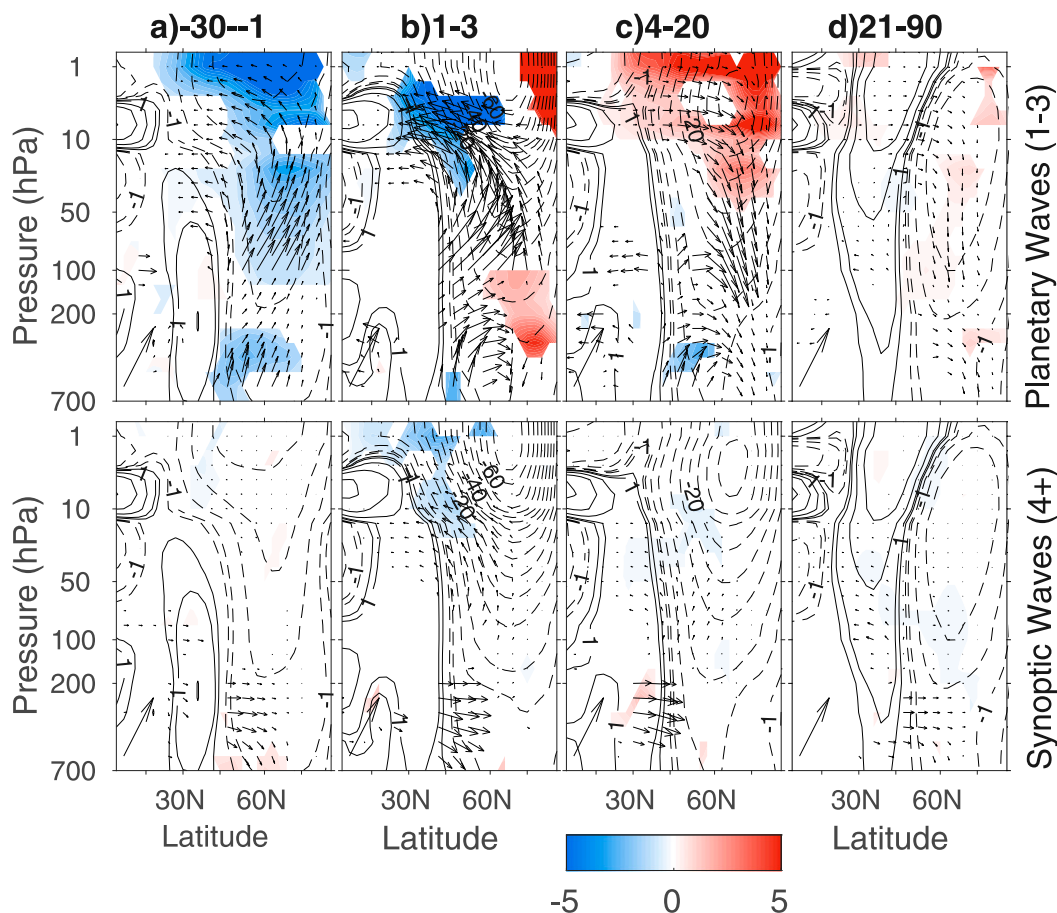
FIG. 6. Latitude–height cross sections of the Eliassen–Palm flux **F** (arrows) and the Eliassen–Palm flux divergence $\Pi = \nabla \cdot \mathbf{F}/\rho_0 a \cos\varphi$ (m s^{-1} day^{-1}; shading) anomalies averaged over various lag stages in CTRL, and filtered for (top) planetary waves 1–3 and (bottom) synoptic waves 4+. A lower level of 700 hPa is used here to avoid complications with topography when calculating the eddy contributions to **F** in Eqs. (5) and (6). Stratospheric arrows are scaled by a factor of 5 to aid in visualization. Thin black contours are as in Fig. 2. Note that only **F** vectors for which either of its components is statistically significant are plotted. The lag stages that are averaged over are indicated at the top of each column.

momentum fluxes (e.g., Limpasuvan et al. 2004; Song and Robinson 2004; Domeisen et al. 2013; Hitchcock and Simpson 2014).

We now compare the anomalies in the CTRL SSWs with those for the 15-K PTRB in Fig. 7, which shows the same as Fig. 6 except without panels at negative lags. At lags 1–3 (Fig. 7a), a vertical dipole in Π for planetary waves is evident, which straddles the lowest level of maximum forcing at ~60 hPa, with anomalous divergence aloft, and convergence extending down to ~200 hPa. This dipole is associated with anomalous downward-propagating planetary waves and occurs as a direct response to the weakened vortex. In particular, the weakening vortex lowers the critical lines and hence prevents Rossby waves from propagating freely. The increase in static stability associated with the thermal forcing may also play a role in

reducing the upward propagation of planetary waves [see Eq. (5b) and Chen and Robinson 1992]. This will also be explained by refractive index arguments in section 3c. In the region of anomalous tropospheric $\bar{u} > 0$, there is anomalous weak-valued synoptic waves that propagate upward and converge in the lower stratosphere, consistent with the larger propagation window for smaller-scale waves (see Charney and Drazin 1961).

At lags 4–20 (i.e., after the forcing has been switched off; Fig. 7b), the planetary wave anomalies are more widespread with an anomalous poleward and downward propagation extending from the stratospheric subtropics down to the high-latitude troposphere and with divergence aloft and convergence in the lower stratosphere–upper troposphere. In particular, the **F** anomalies extend down to 700 hPa in conjunction with
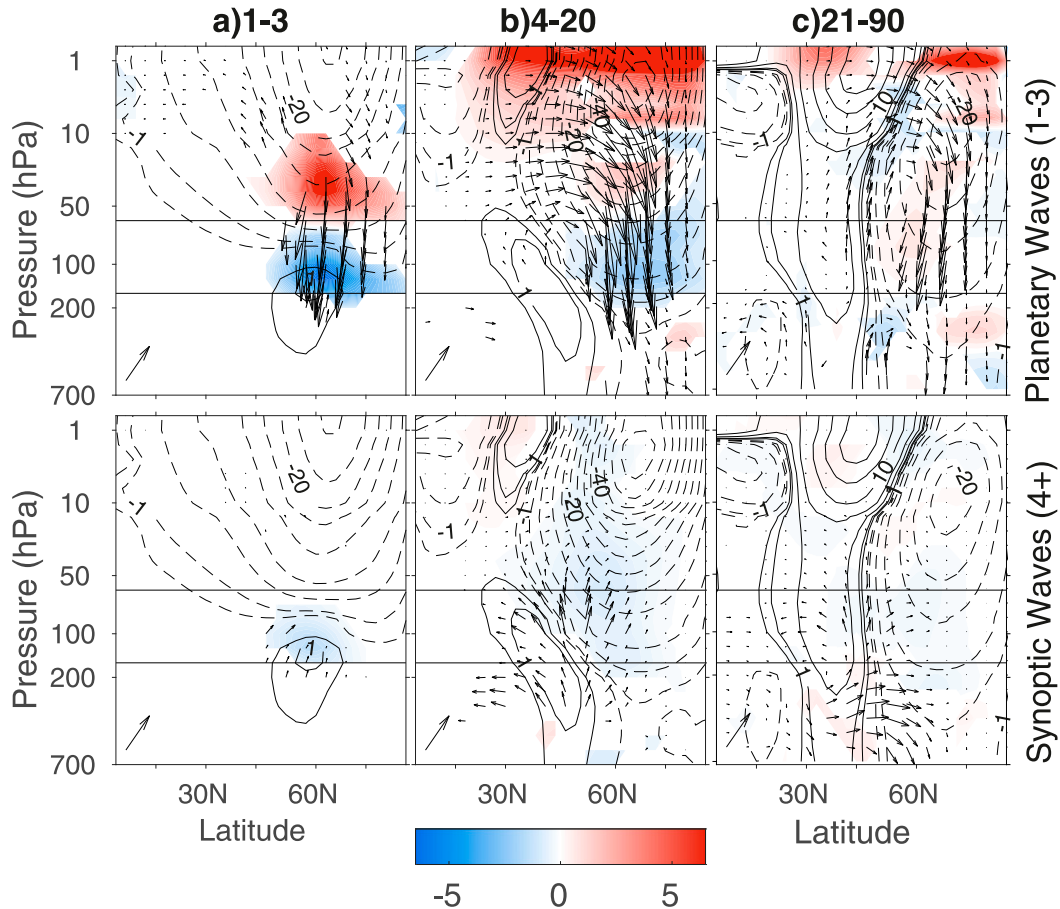
FIG. 7. As in Fig. 6, but for the 15-K PTRB and with the omission of the panels at negative lags. Thin horizontal lines are as in Fig. 1a.

the $\overline{u} < 0$ anomalies at high latitudes. In terms of synoptic waves, a fountain of anomalies is apparent at midlatitudes with convergence in the stratosphere. These anomalous synoptic waves may originate due to the enhanced baroclinicity associated with the anomalous tropospheric westerlies but are also consistent with the enhanced ability to propagate into the stratosphere as the vortex weakens.

At lags 21–90 (Fig. 7c), both the planetary wave and synoptic wave anomalies are similar to those in CTRL (Fig. 6). The planetary wave anomalies are essentially the same as at earlier lags, but with weaker magnitude as the vortex recovers. In terms of synoptic waves, there are clear poleward-propagating anomalies straddling the tropospheric $\overline{u}$ dipole, necessary to maintain the $\overline{u}$ anomalies against surface friction.

We next investigate the source of the tropospheric poleward-propagating synoptic waves. In Fig. 8a, a latitudinal profile of the Eady growth rate ($\sigma = 0.31|f||\partial u(\varphi, z, t)/\partial z|/N$) anomalies (Hoskins and Valdes 1990, blue line) at 400 hPa, averaged over lags 21–90 is shown for

the 15-K PTRB. Also shown are the corresponding 400-hPa $\overline{u}$ (black line) and synoptic wave $F^{(z)}$ (red line) anomalies. Note that similar results are obtained at other tropospheric levels. At midlatitudes (high latitudes), the dipole of $\overline{u} > 0$ ($\overline{u} < 0$) anomalies is collocated with $F^{(z)} > 0$ ($F^{(z)} < 0$) and $\sigma > 0$ ($\sigma < 0$). This suggests that in the midlatitude region of enhanced baroclinicity, there is an enhanced generation of synoptic waves, in contrast to at higher latitudes, where generation is reduced. Although it is difficult to establish conclusively from the EP fluxes and Eady growth rate alone, these upward-propagating synoptic waves propagate poleward and drive the persistent jet shift (Fig. 7) in a positive feedback as suggested by Robinson (2000) and Song and Robinson (2004). The midlatitude region of $\sigma > 0$ is located farther poleward at earlier lags and migrates equatorward alongside the $\overline{u}$ anomalies (not shown).

To provide further evidence that the poleward-propagating synoptic waves break at subpolar latitudes, the total wavenumber
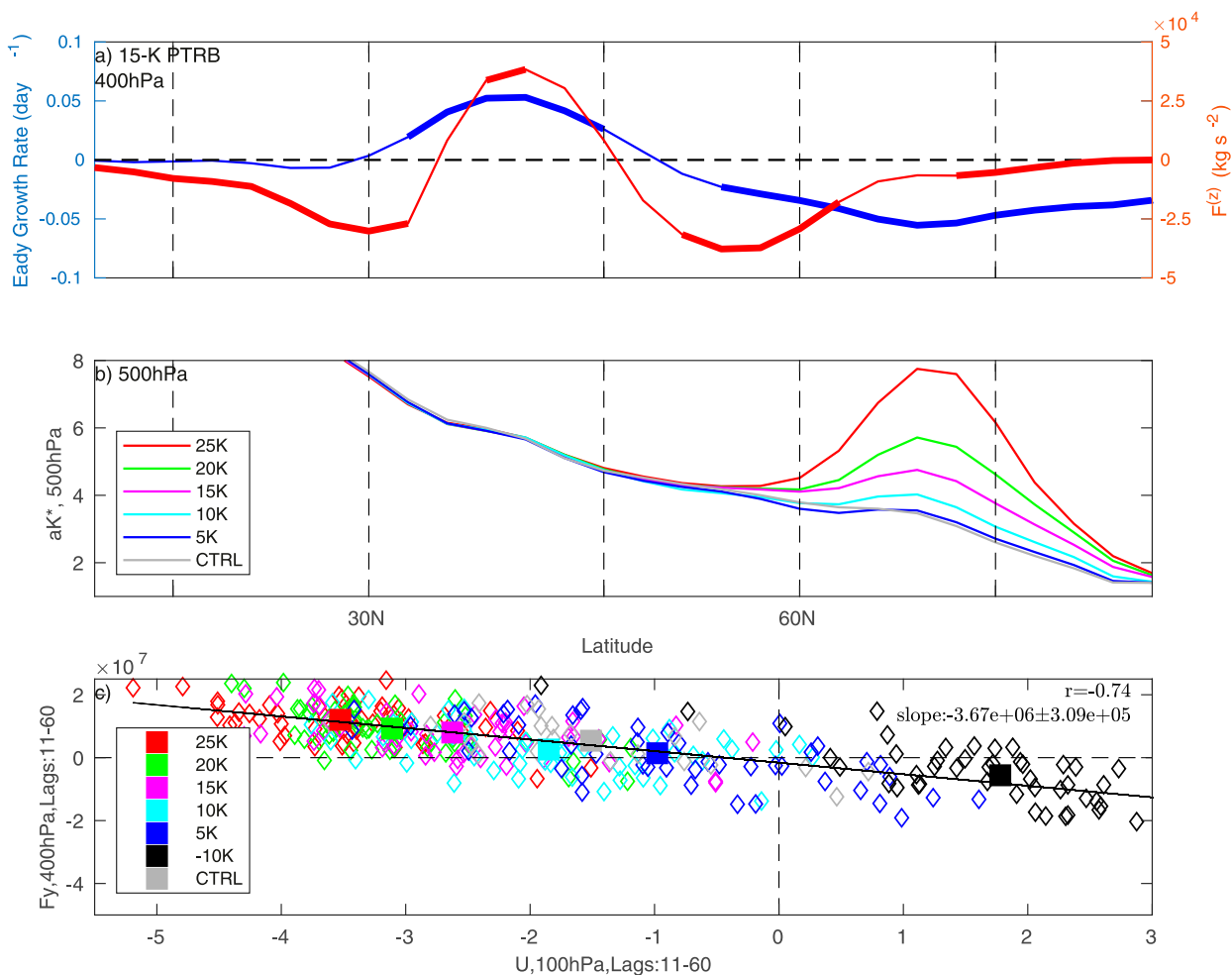
FIG. 8. (a) Latitudinal profile of the Eady growth rate σ (blue line; day^{-1}) and synoptic wave $F^{(z)}$ (red line) anomalies at 400 hPa and averaged over lags 21–90 for the 15-K PTRB. Double-thickness lines indicate statistically significant differences from CTRL at the 95% level. (b) Latitudinal profiles of the total wavenumber K^* (with $c = 0$ and multiplied by Earth's radius) at 500 hPa for all PTRB heating experiments. The DJF climatological aK^* for CTRL is also plotted in gray. (c) Scatterplot of $\overline{u}$ at 100 hPa and averaged over 60°–87°N and lags 11–60 (m s^{-1}), against the synoptic wave $F^{(\varphi)}$ at 400 hPa, averaged over 45°–55°N and over lags 11–60. The correlation coefficient and regression slope are included in the top right of (c).

$$K^* = \cos\varphi \left(\frac{\beta^*}{\overline{u} - c} \right), \qquad (8)$$

(Hoskins and Karoly 1981) as a function of latitude at 500 hPa is plotted in Fig. 8b for all PTRB experiments averaged over lags 21–90 (we assume $c = 0^1$). In Eq. (8), β^* is the meridional derivative of the absolute vorticity in spherical coordinates. This diagnostic shows that a

Rossby wave will be turned at a latitude where $k = K^*$ (i.e., where the meridional wavenumber becomes zero), will propagate toward regions of larger K^*, before breaking at a critical latitude at which $\overline{u} = c$ and K^* becomes infinite. South of ~55°N, the DJF-climatological K^* in CTRL (gray line) and PTRB K^* (colored lines) are essentially inseparable. However, in the region of easterly $\overline{u}$ anomalies farther poleward, the PTRB experiments diverge from the CTRL with a K^* peak at ~65°N. For stronger heating, this peak in K^* becomes more prominent toward higher wavenumbers. In the region of the K^* peak, linear theory suggests that meridionally propagating synoptic waves are essentially trapped due to the presence of turning latitudes on both the poleward and equatorward flanks (evidenced by $K^* \to 0$) and will eventually break.

---

[1] Note that upon including $c > 0$, the K^* peak is evident at subpolar latitudes (see below), but north of ~60°N, K^* becomes imaginary (and hence represents wave evanescence). To better highlight the peak at subpolar latitudes therefore, we use a value of $c = 0$.

Note that the peak becomes more pronounced and extends to higher zonal wavenumbers at lower levels (not shown). The increase in K^* for stronger PTRB experiments indicates that a stronger stratospheric warming leads to a stronger synoptic wave response.

It is next shown that the magnitude of the lower-stratospheric anomalies influence the strength of the tropospheric synoptic-wave anomalies. Figure 8c shows a scatter graph of the 100-hPa high-latitude $\overline{u}$ averaged over lags 11–60 plotted against the synoptic wave $F^{(\varphi)}$ at 400 hPa and averaged over 45°–55°N and lags 11–60. Note that the results in the scatterplot are not sensitive to variations in the averaging lags or latitudes. Overall, the correlation coefficient between the two is $r = -0.74$, indicating a fairly strong linear relationship (i.e., a stronger stratospheric temperature perturbation likely gives rise to a stronger tropospheric eddy momentum flux response, although the direction of causality cannot be inferred just from the correlation analysis presented here). Nevertheless, there is much variability in terms of individual ensemble members (colored diamonds). The linearity of the tropospheric and stratospheric response is also shown in time series plots of $F^{(\varphi)}$ and $F^{(z)}$ (Figs. S3a,b).

Overall, it appears that poleward-propagating synoptic waves play a key role in the maintenance of the equatorward-shifted tropospheric jet at longer lags in both the CTRL and PTRB SSWs (in contrast to equatorward-propagating synoptic waves in the PTRB cooling experiment). Such waves appear to be generated by the enhanced baroclinicity at midlatitudes, and propagate poleward where they break in the region of easterly anomalies (see Fig. S3c for evidence of EP flux convergence at high latitudes). Planetary waves on the other hand, are suppressed throughout the stratosphere and troposphere and may play a key role at short lags in initially bringing the polar vortex anomalies to the troposphere; however, examination of the initial downward communication is left to a future study.

c. Waveguide evolution

To determine if the changes in wave propagation shown in section 3b are consistent with that expected due to wave refraction in response to the evolving zonal-mean basic state, we now examine the refractive index:

$$n^2 = \frac{1}{\overline{u}-c} \overbrace{\left\{ 2\Omega\cos\varphi - \left[\frac{(\overline{u}\cos\varphi)_\varphi}{a\cos\varphi}\right]_\varphi - \frac{a}{\rho_0}\left(\frac{\rho_0 f^2}{N^2}\overline{u}_z\right)_z \right\}}^{\equiv \overline{q}_\varphi} - \frac{k^2}{a^2\cos^2\varphi} - \frac{f^2}{4N^2 H^2}$$

(9)

(e.g., Matsuno 1970) where $\overline{q}_\varphi$ is the meridional gradient of quasigeostrophic potential vorticity (PV), N^2 is the static stability, k is the zonal wavenumber, c is the phase speed, H is the density scale height, and all remaining variables are as in earlier equations. Even though strictly speaking, the refractive index can only predict wave behavior in the Wentzel–Kramers–Brillouin (WKB) limit, many previous studies have shown that the refractive index can provide useful information despite the fact that their experiments may not satisfy the underlying assumptions (e.g., Chen and Robinson 1992; Simpson et al. 2009; Garfinkel et al. 2012). It is expected in this framework that waves tend to preferentially propagate away from regions of small n^2 toward regions of larger n^2. Waves cannot propagate in regions of $n^2 < 0$. Close to a critical line (where $\overline{u} = c$), n^2 becomes extremely large.

To calculate n^2 for the CTRL SSWs, we first average $\overline{u}(\varphi, z, t)$ and N^2 over the required lag stages and over all SSWs. Then N^2 is further averaged vertically in the stratosphere (after pressure weighting), although using an N^2 profile that varies with height does not change the results qualitatively. The n^2 and $\overline{q}_\varphi$ anomalies for CTRL shown in Fig. 9 (top) are then calculated by subtracting the December–February climatology of n^2 and $\overline{q}_\varphi$. Note that in difference plots such as those presented here, the latter two terms in Eq. (9) cancel out and hence the anomalies are the same for all wavenumbers. Note that $c = 0$ is used in Eq. (9). The calculation of n^2 and $\overline{q}_\varphi$ for the PTRB experiments are calculated similarly except that N^2 is averaged over December–May (i.e., the length of each PTRB ensemble member) and over all ensemble members, and the anomalies are calculated as deviations from the corresponding lags in the CTRL daily climatology.

Figure 9 shows composites of n^2 and $\overline{q}_\varphi$ anomalies averaged over the same lags as in Fig. 2 for the CTRL SSWs (top) and for the 15-K PTRB (bottom). Note that the full field for both CTRL and PTRB is provided in Fig. S2. Focusing first on the CTRL SSWs (Fig. 9, top), one of the most noticeable features is the high-latitude tropospheric region of anomalous $n^2 > 0$, associated with the tropospheric $\overline{u}$ anomalies (Fig. 2). This $n^2 > 0$ feature would be expected to encourage wave propagation toward it, as indeed seen in Fig. 6 with anomalous planetary wave $F^{(z)} < 0$ and anomalous tropospheric synoptic wave $F^{(\varphi)} > 0$. Aloft, the weakening vortex is indicated by negative $\overline{q}_\varphi$ anomalies. Note that there does not appear to be any preferential cavity for enhanced upward wave propagation prior to the onset, in the sense of focusing planetary waves onto the pole.

A developing feature at positive lags is a region of $n^2 < 0$ in the midlatitude–subpolar upper troposphere–lower
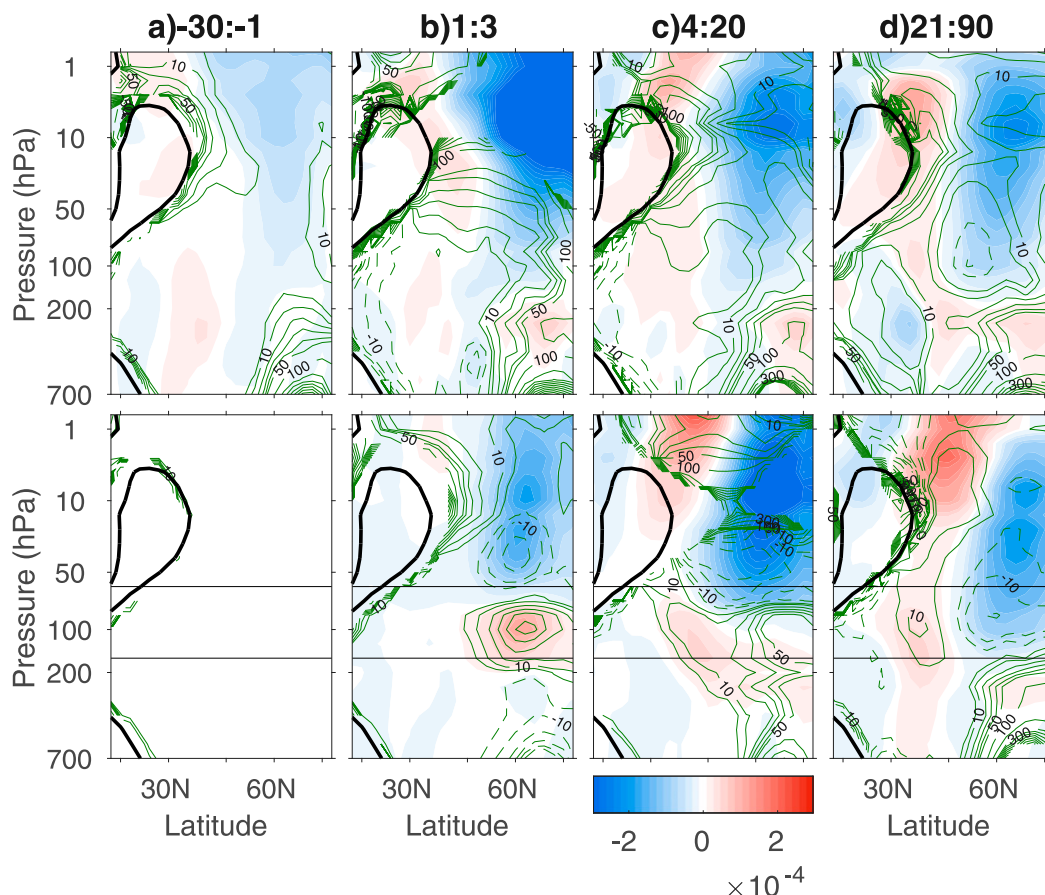
FIG. 9. Quasigeostrophic refractive index n^2 (contours) and potential vorticity gradient $\overline{q}_\varphi$ (shading) anomalies averaged over various lag stages for (top) CTRL and (bottom) the 15-K PTRB experiment. Solid (dashed) green contours indicate positive (negative) n^2 anomalies. Note that n^2 has been scaled by a^2 and is hence dimensionless, whereas $\overline{q}_\varphi$ has units of s^{-1}. Contours of n^2 are at $\pm100, 200, \ldots, 1000$ with additional contours at $\pm5, 10, 20, \ldots, 50$. Also, note that n^2 contours have been omitted where $\overline{u} < 0$ (N.B. that $\overline{u}$ in this case is the full field and not the anomaly). See text for details regarding the calculations for both CTRL and PTRB. The thick black line is the December–February climatological zero-wind line. Horizontal lines in the bottom row are as in Fig. 1a.

stratosphere, which intensifies as the lags progress. Upon comparison with the December–February climatology of n^2 (see Fig. S1b), it appears that this feature extends the subtropical–midlatitude minimum of n^2 to higher latitudes, and hence, may act to shield the stratosphere from subsequent upward wave propagation. Nevertheless, we note that tunneling of planetary waves through a region of $n^2 < 0$ is still possible (e.g., Harnik 2002). Above ~50 hPa, n^2 becomes positive after lags 1–3, as the vortex starts to recover (i.e., $\overline{u}$ returns to positive).

We now examine the PTRB SSWs (Fig. 9, bottom). First note that at negative lags (Fig. 9a), the presence of n^2 anomalies close to the zero-wind line represent floating point errors due to the very small $\overline{u}$ in this region. During the forcing stage (Fig. 9b; lags 1–3), the n^2 anomalies exhibit a vertical tripole in the extratropics,

with an $n^2 > 0$ anomaly from the upper troposphere to lower stratosphere, and $n^2 < 0$ both above and below. This vertical tripole is the perhaps expected response given the high-latitude thermal forcing. Note that the region of anomalous high-latitude tropospheric $n^2 < 0$ occurs due to the vertical curvature associated with the anomalous tropospheric westerlies slightly aloft (see Fig. 2b). The negative (positive) PV gradient in the middle–upper (lower) stratosphere is also the expected response given the forcing. These n^2 anomalies agree dynamically with the **F** anomalies in the top row of Fig. 7, whereby there is convergence in the region of $n^2 > 0$ and divergence above and below.

At lags 4+ (Figs. 9c,d), n^2 and and $\overline{q}_\varphi$ become rather similar to in CTRL. In particular, the region of $n^2 < 0$ in the middle-to-lower stratosphere develops and becomes larger in magnitude as the lags progress. In the

high-latitude troposphere, the region of anomalous $n^2 < 0$ at lags 1–3, completely switches sign to $n^2 > 0$. This region of $n^2 > 0$ becomes larger in magnitude as the lags progress, occurring in response to the $\overline{u} < 0$ anomalies associated with the weaker vortex aloft, which have started their descent to the troposphere, and due to the fact that the tropospheric $\overline{u} > 0$ anomalies have shifted more equatorward. As aforementioned, these two features act to shelter the stratosphere from further upward planetary wave propagation and to encourage enhanced poleward wave propagation (Fig. 7). The poleward-propagating synoptic waves may indeed play a role in the intensification of this feature, via a positive feedback: poleward synoptic waves flux momentum equatorward that intensifies the easterly anomalies at high latitudes, and thus intensifies the ambient refractive index (the high-latitude westerlies do not actually reverse; not shown). Consequently, this encourages farther poleward synoptic wave propagation.

Overall, as was the case in sections 3a and 3b, after ~3 weeks, the n^2 anomalies in the thermally forced SSWs become similar to those in the CTRL SSWs. In particular, the mid- to high-latitude lower-tropospheric $n^2 > 0$, the midlatitude lower-stratospheric $n^2 < 0$, and the large positive n^2 above ~50 hPa, are all common features to CTRL and PTRB. The EP fluxes in section 3b agree dynamically with the n^2 anomalies here, and in particular, the high-latitude tropospheric region of $n^2 > 0$ first develops in response to the downward migration of the stratospheric $\overline{u}$ from aloft, before intensifying in an apparent positive feedback with the (likely) baroclinically induced poleward-propagating synoptic waves.

d. Meridional circulation evolution

Wave activity propagation and forcing is intimately linked to the meridional circulation. To examine the evolution of the meridional circulation during SSWs in relation to the wave-forcing anomalies in the previous section, we examine the residual meridional mass streamfunction:

$$\Psi^* = \int_z^\infty \rho_0 \overline{v}^* \cos\varphi \, dz = \int_z^\infty \rho_0 \left[\overline{v} - \frac{1}{\rho_0} \frac{\partial}{\partial z} \frac{\rho_0 \overline{v'\theta'}}{\overline{\theta}_z} \right] \cos\varphi \, dz$$

$$= \int_z^\infty \rho_0 \overline{v} \cos\varphi \, dz + \frac{\rho_0 \overline{v'\theta'}}{\overline{\theta}_z} \cos\varphi \equiv \Psi_{\overline{v}} + \Psi_{\overline{v'\theta'}},$$

(10)

which approximates the Lagrangian-mean circulation of air parcels [e.g., Andrews et al. 1987, and see Eq. (7)]. The terms $\Psi_{\overline{v}}$ and $\Psi_{\overline{v'\theta'}}$ represent the Eulerian-mean meridional circulation and eddy heat flux contributions to Ψ^*, respectively, and are

presented in Figs. S4 and S5. We present the evolution of Ψ^* during SSWs.

Figure 10 (top) shows composites of Ψ^* at various lag stages for the CTRL SSWs. At negative lags (Fig. 10a), Ψ^* is everywhere positive indicative of a strengthened Brewer–Dobson circulation during the lead up to an SSW. This is driven by an imbalance between the enhanced upward-propagating planetary wave activity ($\Psi_{\overline{v'\theta'}} > 0$) and the induced thermally indirect equatorward Eulerian-mean circulation ($\Psi_{\overline{v}} < 0$; not shown). The latter, upon being influenced by the Coriolis force, yield the easterly $\overline{u}$ anomalies associated with the weakened polar vortex (Matsuno 1971). At lags 1–3, the stratosphere still has a strengthened Brewer–Dobson circulation (de la Camara et al. 2018), although at lags 4+, these positive anomalies become weakly negative, due to the cutoff of planetary waves (see Fig. 6).

The tropospheric Ψ^* response at positive lags is an extratropical tripole with $\Psi^* > 0$ at midlatitudes flanked at low and high latitudes by $\Psi^* < 0$ (although the high-latitude cell is much weaker at lags 4+). This tripole corresponds to changes in the width of the polar, Ferrel, and Hadley cells (e.g., Martineau et al. 2018). Indeed, this tripole is the response associated with general stratospheric NAM variability rather than variability solely attributed to the tropospheric NAM (see Fig. S6). We note that the $\Psi^* < 0$ anomalies at ~30°–45°N and the $\Psi^* > 0$ anomalies at ~45°–65°N straddle the nodal line in $\overline{u}$ and represent the meridional circulation response to the synoptic-wave $F^{(\varphi)} > 0$ (i.e., $\overline{u'v'} < 0$) forcing anomalies (Fig. 6) that drive the zonal-mean state away from thermal wind balance and necessitate the development of a pair of meridional circulation cells.

The bottom row of Fig. 10 shows Ψ^* anomalies for the 15-K PTRB experiment. Note that Ψ^* is qualitatively similar for all of our experiments. At lags 1–3 (i.e., during the forcing stage; Fig. 10b), Ψ^* is everywhere negative, with largest magnitudes at ~55°N, ~50 hPa, and a second peak at ~45°N, 500 hPa. The $\Psi_{\overline{v}}$ contribution dominates Ψ^* with $\Psi_{\overline{v}} < 0$ everywhere (not shown); this is the expected response and is similar to the instantaneous response to a diabatic heating anomaly found in Shepherd et al. (1996) (their Fig. 2a), although their heating was centered at midlatitudes and hence had a weaker secondary circulation cell at higher latitudes. In particular, the imposed diabatic heating anomaly is balanced by rising motion over the pole, and descending motion farther equatorward, which by mass continuity gives rise to poleward (equatorward) motion in the upper troposphere (upper stratosphere). The contribution of $\Psi_{\overline{v'\theta'}}$ is that of a dipole straddling the lowest level of forcing (lower horizontal line; as in Fig. 7).
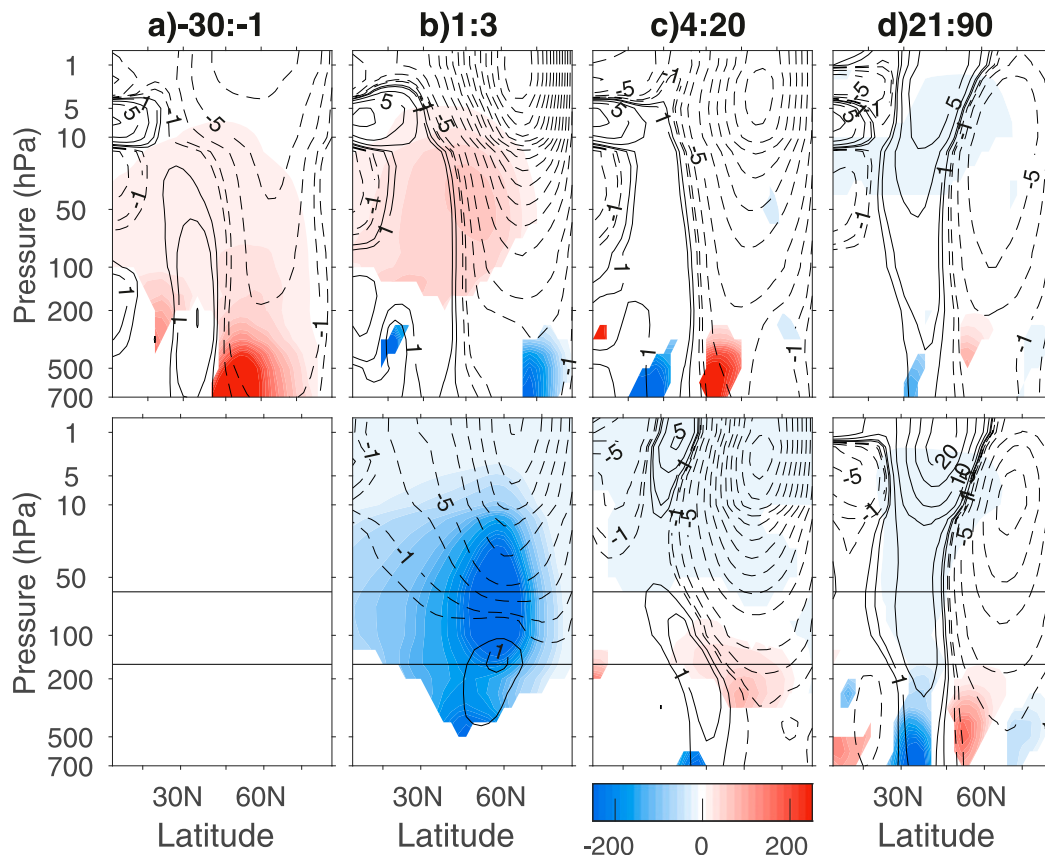
FIG. 10. Latitude–height cross sections of the residual mean meridional circulation Ψ^* (kg m s^{-2}), averaged over lags (a) from -30 to 1, (b) 1–3, (c) 4–20, and (d) 21–90 for the (top) CTRL and (bottom) 15-K PTRB experiment. Note that the two lag stages 4–10 and 11–20 in Fig. 2 have been averaged into a single panel here, for brevity. Note that only Ψ^* anomalies that are statistically significantly different from the climatology in CTRL are shaded. Black contours represent the corresponding $\bar{u}$ anomalies at these lags with contours at $\pm 0.5, 1, 2.5, 5, 10, \ldots$ m s^{-1}.

At lags 4–20 (Fig. 10c), the Ψ^* anomalies are noticeably different to those in CTRL. For instance, the anomalous meridional circulation between ~ 400 and ~ 50 hPa completely reverses to $\Psi^* > 0$. This occurs due to a slight imbalance between $\Psi_{\bar{v}} > 0$ and $\Psi_{\overline{v'\theta'}} < 0$ (not shown). Below 400 hPa, there are insignificant $\Psi^* < 0$ anomalies.

However, by lags 21–90, the Ψ^* anomalies appear to be very similar to those in CTRL, with an extratropical tripole in the troposphere and with weakly negative stratospheric anomalies. The tripole is the response to general stratospheric NAM variability and gives rise to changes in the width of the Ferrel cell, whereas the weakly negative Ψ^* aloft is the response to the reduced upward-propagating planetary waves into the stratosphere (Fig. 7). Hence, after ~ 3 weeks, the circulation following the CTRL SSWs and that following the thermally forced SSWs in PTRB become very similar to one another.

In summary, there are large differences in Ψ^* between the CTRL SSWs and the thermally forced SSWs

at lags of less than ~ 3 weeks. However, at longer lags, the Ψ^* anomalies evolve very similarly with a tropospheric tripole associated with the shifted jet, and a weakly negative stratospheric Ψ^* associated with the suppressed planetary waves following the SSW onset (see section 3b).

4. Summary and discussion

We have examined the tropospheric response to varying magnitude high-latitude stratospheric heating perturbations in order to examine the downward influence of SSWs. To capture the sudden nature of an SSW, the heating perturbation was only switched on for a few days (spun off from a free-running control integration, CTRL), which, depending on the magnitude of the imposed heating, either gave rise to a weakened, or completely reversed vortex. The evolution of the thermally forced SSWs was then compared with naturally occurring SSWs identified in CTRL. Our novel approach

has allowed us to isolate the tropospheric response associated with the weakened polar vortex, as opposed to the response associated with the original planetary waves (and hence momentum torques) that initiated the SSW. We have focused in particular on understanding the long-lag (i.e., >2–3 weeks) tropospheric response as opposed to the initial communication of the stratospheric anomalies to the troposphere at shorter lags.

Our results confirm a downward influence from the stratosphere following an SSW event (e.g., Baldwin and Dunkerton 2001). This is evidenced by the strong tropospheric signal following the thermally forced SSWs (Figs. 2–5) despite the fact that there are no momentum torques associated with preceding planetary waves that initiate the SSW (as is the case in the free-running CTRL SSWs). Plumb and Semeniuk (2003) demonstrated that the tropospheric zonal-wind anomalies following a SSW could occur passively in response to the upward-propagating planetary waves that initiated the SSW, and hence concluded that a downward migration of wind anomalies is not necessarily indicative of a downward stratospheric influence. Our results unambiguously confirm that a weakening of the stratospheric polar vortex drives a tropospheric circulation response.

Another key result is that at longer lags, the stratospheric and tropospheric evolution in the free-running CTRL SSWs and the thermally forced SSWs are remarkably similar, both in terms of the zonal-mean circulation and the eddy fluxes (Figs. 2, 6, 7, 9, and 10). This indicates that at longer lags the tropospheric response is somewhat generic and the initial formation of an SSW does not play a large role. Instead, the strength of the warming in the lower stratosphere determines the magnitude of the tropospheric response (Fig. 5, and in agreement with, e.g., Maycock and Hitchcock 2015). In particular, our results indicate a robust linear relationship between the strength of the lower-stratospheric warming and the tropospheric response, with the linearity also extending to sudden stratospheric cooling events (Figs. 5 and 8). The linear response rules out the presence of any regime-like tropospheric behavior (at least in MiMA). Nevertheless, at shorter lags, the particulars associated with the initial SSW formation may play a potentially important role, given the difference in evolution between the CTRL SSWs and PTRB SSWs.

In maintaining the tropospheric jet shift at longer lags, synoptic waves play a key role (see Figs. 6–8), in agreement with a number of studies (e.g., Limpasuvan et al. 2004; Polvani and Waugh 2004; Song and Robinson 2004; Domeisen et al. 2013). The collocation of upward-propagating synoptic waves and the peak Eady growth rate in the region of midlatitude westerly anomalies

suggests that synoptic waves may be forced due to the enhanced baroclinicity (see Fig. 8 and e.g., Robinson 2000). The poleward propagation of these synoptic waves then appears to generate a positive feedback in concert with the region of enhanced high-latitude tropospheric refractive index that develops in response to the descending polar vortex anomalies and intensifies as the lags progress (Fig. 9). In particular, the poleward-propagating synoptic waves flux momentum equatorward [see Eq. (5a)] and thus weaken the winds further at high latitudes, which in turn enhances the ambient refractive index [due to $\bar{u} - c$ in the denominator of Eq. (10)] and subsequently encourages more poleward synoptic wave propagation. This explanation is similar to that in Simpson et al. (2009), who suggest a change in the refractive index to initiate changes in momentum fluxes that feed back on the ambient refractive index. We note that the poleward-propagating synoptic waves and n^2 feature were also present at all lags in CTRL; at negative lags it was associated with the tropospheric precursors. However, whether this feedback mechanism plays a role during observed SSWs requires further work.

The initial 3-week period after 1 January in the PTRB experiments during which the polar-vortex anomalies migrate downward to the surface, requires further investigation. The circulation anomalies gradually propagate down to ~300 hPa over the first ~2 weeks, before they barotropically extend downward to the high-latitude lower troposphere (Fig. 3). The suppression of planetary waves appears to correlate with this downward propagation (Fig. 7) in agreement with Hitchcock and Haynes (2016) and Hitchcock and Simpson (2016). Once the mean-state anomalies reach the lower troposphere, they subsequently migrate equatorward before stalling at midlatitudes where they straddle the midlatitude jet (Figs. 2 and 4). The exact mechanisms for this downward and subsequently equatorward migration of the winds is beyond the scope of this paper, although we note that both the CTRL and PTRB SSWs exhibit anomalous wave convergence into the polar cap at lags of 4–20 (Figs. 6 and 7), which may play a role in the initial downward communication.

Unlike in our CTRL run (as well as in observations), for which the near-surface response following an SSW projects almost entirely onto the first EOF, the near-surface response following the PTRB SSWs projects onto both the first and second EOFs (Fig. 4), although with a larger projection onto EOF1. Parallels can therefore be drawn between the PTRB SSWs and the observed response during final warmings, which have been found in observations to project onto both leading EOFs (e.g., Black et al. 2006; Sheshadri et al. 2017),

JOURNAL OF CLIMATE

although we note that in our PTRB runs, the winds do reverse back to westerly. Hence, our experiments may be useful for examining the tropospheric response to a wide range of polar vortex variability.

It should be noted that the mechanisms for downward propagation discussed here are based on the evolution during thermally triggered SSWs, which, by construction, lack the vital ingredient of planetary-scale momentum torques that are ultimately responsible for observed SSWs. The meridional circulation anomalies associated with heating and momentum torques can be very different (e.g., Shepherd et al. 1996) and hence could conceivably have different effects on the troposphere. Nevertheless, given the similar evolution of the thermally forced SSWs to the CTRL SSWs at longer lags, these initial momentum torques seemingly do not play a large role in the tropospheric response at subseasonal to seasonal time scales.

One of the advantages of MiMA used here is that it has a realistic stratosphere and annual cycle due to the incorporation of a full radiation scheme (Jucker and Gerber 2017). It is therefore a more realistic setup than that used in previous studies (e.g., Polvani and Kushner 2002; Kushner and Polvani 2004) that have utilized dry dynamical cores with Newtonian cooling. Nevertheless, we note that the annular mode time scales in our presented T42 PTRB experiments are too long compared to our CTRL SSWs (Fig. 3). However, as the results are qualitatively similar to T85 experiments (which have similar annular-mode time scales to in CTRL), our conclusions are unchanged and the essential dynamics are the same.

It has been suggested that the strength of the original wave driving can be important for the tropospheric response to some SSWs (e.g., Nakagawa and Yamazaki 2006; White et al. 2019). This is somewhat similar to the strength of the lower-stratospheric warming in our study. It has also been suggested that the troposphere may need to be in a state to ''receive'' the stratospheric influence (e.g., Black and McDaniel 2004). We agree that the details of an SSW are important for the evolution of an SSW, as well as for the initial downward impact on the troposphere, but argue that the long-lag response of the tropospheric jet is a generic response to a weakened polar vortex.

REFERENCES

Alexander, M., and T. J. Dunkerton, 1999: A spectral parameterization of mean-flow forcing due to breaking gravity waves. *J. Atmos. Sci.*, **56**, 4167–4182, https://doi.org/10.1175/1520-0469(1999)056<4167:ASPOMF>2.0.CO;2.

Ambaum, M. H. P., and B. J. Hoskins, 2002: The NAO troposphere–stratosphere connection. *J. Climate*, **15**, 1969–1978, https://doi.org/10.1175/1520-0442(2002)015%3C1969:TNTSC%3E2.0.CO;2.

Andrews, D. G., J. R. Holton, and C. B. Leovy, 1987: *Middle Atmosphere Dynamics*. Academic Press, 489 pp.

Baldwin, M. P., and T. J. Dunkerton, 1999: Propagation of the Arctic oscillation from the stratosphere to the troposphere. *J. Geophys. Res.*, **104**, 30 937–30 946, https://doi.org/10.1029/1999JD900445.

——, and ——, 2001: Stratospheric harbingers of anomalous weather regimes. *Science*, **294**, 581–584, https://doi.org/10.1126/science.1063315.

——, and D. W. J. Thompson, 2009: A critical comparison of stratosphere-troposphere coupling indices. *Quart. J. Roy. Meteor. Soc.*, **135**, 1661–1672, https://doi.org/10.1002/qj.479.

Betts, A., 1986: A new convective adjustment scheme. Part I: Observational and theoretical basis. *Quart. J. Roy. Meteor. Soc.*, **112**, 677–691, https://doi.org/10.1002/QJ.49711247307.

——, and M. Miller, 1986: A new convective adjustment scheme. Part II: Single column tests using GATE wave, BOMEX, ATEX and Arctic air-mass data sets. *Quart. J. Roy. Meteor. Soc.*, **112**, 693–709, https://doi.org/10.1002/QJ.49711247308.

Black, R. X., and B. A. McDaniel, 2004: Diagnostic case studies of the northern annular mode. *J. Climate*, **17**, 3990–4004, https://doi.org/10.1175/1520-0442(2004)017<3990:DCSOTN>2.0.CO;2.

——, ——, and W. A. Robinson, 2006: Stratosphere–troposphere coupling during spring onset. *J. Climate*, **19**, 4891–4901, https://doi.org/10.1175/JCLI3907.1.

Butler, A. H., D. W. J. Thompson, and R. Heikes, 2010: The steady-state atmospheric circulation response to climate change–like thermal forcings in a simple general circulation model. *J. Climate*, **23**, 3474–3496, https://doi.org/10.1175/2010JCLI3228.1.

Charlton, A. J., and L. M. Polvani, 2007: A new look at stratospheric sudden warmings. Part I: Climatology and modeling benchmarks. *J. Climate*, **20**, 449–469, https://doi.org/10.1175/JCLI3996.1.

Charney, J. G., and P. G. Drazin, 1961: Propagation of planetary-scale disturbances from the lower into the upper atmosphere. *J. Geophys. Res.*, **66**, 83–109, https://doi.org/10.1029/JZ066i001p00083.

Chen, P., and W. A. Robinson, 1992: Propagation of planetary waves between the troposphere and stratosphere. *J. Atmos. Sci.*, **49**, 2533–2545, https://doi.org/10.1175/1520-0469(1992)049<2533:POPWBT>2.0.CO;2.

Cohen, J., and J. Jones, 2011: Tropospheric precursors and stratospheric warmings. *J. Climate*, **24**, 6562–6572, https://doi.org/10.1175/2011JCLI4160.1.

Cohen, N. Y., E. P. Gerber, and O. Buhler, 2014: What drives the Brewer–Dobson circulation? *J. Atmos. Sci.*, **71**, 3837–3855, https://doi.org/10.1175/JAS-D-14-0021.1.

de la Camara, A., M. Abalos, and P. Hitchcock, 2018: Changes in stratospheric transport and mixing during sudden stratospheric

warmings. *J. Geophys. Res. Atmos.*, **123**, 3356–3373, https://doi.org/10.1002/2017JD028007.

Domeisen, D. I. V., L. Sun, and G. Chen, 2013: The role of synoptic eddies in the tropospheric response to stratospheric variability. *Geophys. Res. Lett.*, **40**, 4933–4937, https://doi.org/10.1002/grl.50943.

Frierson, D. M., I. M. Held, and P. Zurita-Gotor, 2006: A gray-radiation aquaplanet moist GCM. Part I: Static stability and eddy scale. *J. Atmos. Sci.*, **63**, 2548–2566, https://doi.org/10.1175/JAS3753.1.

Garfinkel, C. I., D. L. Hartmann, and F. Sassi, 2010: Tropospheric precursors of anomalous Northern Hemisphere stratospheric polar vortices. *J. Climate*, **23**, 3282–3299, https://doi.org/10.1175/2010JCLI3010.1.

——, T. A. Shaw, D. L. Hartmann, and D. W. Waugh, 2012: Does the Holton–Tan mechanism explain how the quasi-biennial oscillation modulates the Arctic polar vortex? *J. Atmos. Sci.*, **69**, 1713–1733, https://doi.org/10.1175/JAS-D-11-0209.1.

——, D. W. Waugh, and E. P. Gerber, 2013: The effect of tropospheric jet latitude on coupling between the stratospheric polar vortex and the troposphere. *J. Climate*, **26**, 2077–2095, https://doi.org/10.1175/JCLI-D-12-00301.1.

——, I. P. White, E. P. Gerber, M. Jucker, and M. Erez, 2020: The building blocks of Northern Hemisphere wintertime stationary waves. *J. Climate*, **33**, 5611–5633, https://doi.org/10.1175/JCLI-D-19-0181.1.

Gerber, E. P., and L. P. Polvani, 2009: Stratosphere–troposphere coupling in a relatively simple AGCM: The importance of stratospheric variability. *J. Climate*, **22**, 1920–1933, https://doi.org/10.1175/2008JCLI2548.1.

——, S. Voronin, and L. P. Polvani, 2008: Testing the annular mode autocorrelation time scale in simple atmospheric general circulation models. *Mon. Wea. Rev.*, **136**, 1523–1536, https://doi.org/10.1175/2007MWR2211.1.

——, and Coauthors, 2010: Stratosphere-troposphere coupling and annular mode variability in chemistry-climate models. *J. Geophys. Res.*, **115**, D00M06, https://doi.org/10.1029/2009JD013770.

Haigh, J. D., M. Blackburn, and R. Day, 2005: The response of tropospheric circulation to perturbations in lower-stratospheric temperature. *J. Climate*, **18**, 3672–3685, https://doi.org/10.1175/JCLI3472.1.

Harnik, N., 2002: The evolution of a stratospheric wave packet. *J. Atmos. Sci.*, **59**, 202–217, https://doi.org/10.1175/1520-0469(2002)059<0202:TEOASW>2.0.CO;2.

Hartley, D. E., J. T. Villarin, R. X. Black, and C. A. Davis, 1998: A new perspective on the dynamical link between the stratosphere and troposphere. *Nature*, **391**, 471–474, https://doi.org/10.1038/35112.

Haynes, P. H., C. J. Marks, M. E. McIntyre, T. G. Shepherd, and K. P. Shine, 1991: On the "downward control" of extratropical diabatic circulations by eddy-induced mean zonal forces. *J. Atmos. Sci.*, **48**, 651–678, https://doi.org/10.1175/1520-0469(1991)048<0651:OTCOED>2.0.CO;2.

Held, I. M., and M. J. Suarez, 1994: A proposal for the intercomparison of the dynamical cores of atmospheric general circulation models. *Bull. Amer. Meteor. Soc.*, **75**, 1825–1830, https://doi.org/10.1175/1520-0477(1994)075<1825:APFTIO>2.0.CO;2.

Hitchcock, P., and I. R. Simpson, 2014: The downward influence of stratospheric sudden warmings. *J. Atmos. Sci.*, **71**, 3856–3876, https://doi.org/10.1175/JAS-D-14-0012.1.

——, and P. H. Haynes, 2016: Stratospheric control of planetary waves. *Geophys. Res. Lett.*, **43**, 11 884–11 892, https://doi.org/10.1002/2016GL071372.

——, and I. R. Simpson, 2016: Quantifying eddy feedbacks and forcings in the tropospheric response to stratospheric sudden warmings. *J. Atmos. Sci.*, **73**, 3641–3657, https://doi.org/10.1175/JAS-D-16-0056.1.

——, T. G. Shepherd, and G. L. Manney, 2013: Statistical characterization of Arctic polar-night jet oscillation events. *J. Climate*, **26**, 2096–2116, https://doi.org/10.1175/JCLI-D-12-00202.1.

Holton, J. R., and H.-C. Tan, 1980: The influence of the equatorial quasi-biennial oscillation on the global circulation at 50 mb. *J. Atmos. Sci.*, **37**, 2200–2208, https://doi.org/10.1175/1520-0469(1980)037<2200:TIOTEQ>2.0.CO;2.

Hoskins, B. J., and D. J. Karoly, 1981: The steady linear response of a spherical atmosphere to thermal and orographic forcing. *J. Atmos. Sci.*, **38**, 1179–1196, https://doi.org/10.1175/1520-0469(1981)038<1179:TSLROA>2.0.CO;2.

——, and P. J. Valdes, 1990: On the existence of storm-tracks. *J. Atmos. Sci.*, **47**, 1854–1864, https://doi.org/10.1175/1520-0469(1990)047<1854:OTEOST>2.0.CO;2.

Iacono, M. J., E. J. Mlawer, S. A. Clough, and J. J. Morcrette, 2000: Impact of an improved longwave radiation model, RRTM, on the energy budget and thermodynamic properties of the NCAR Community Climate Model, CCM3. *J. Geophys. Res.*, **105**, 14 873–14 890, https://doi.org/10.1029/2000JD900091.

Jucker, M., and E. P. Gerber, 2017: Untangling the annual cycle of the tropical tropopause layer with an idealized moist model. *J. Climate*, **30**, 7339–7358, https://doi.org/10.1175/JCLI-D-17-0127.1.

——, S. Fueglistaler, and G. K. Vallis, 2013: Maintenance of the stratospheric structure in an idealized general circulation model. *J. Atmos. Sci.*, **70**, 3341–3358, https://doi.org/10.1175/JAS-D-12-0305.1.

Karpechko, A. Y., P. Hitchcock, D. H. W. Peters, and A. Schneidereit, 2017: Predictability of downward propagation of major sudden stratospheric warmings. *Quart. J. Roy. Meteor. Soc.*, **143**, 1459–1470, https://doi.org/10.1002/qj.3017.

Kidston, J., A. A. Scaife, S. C. Hardiman, D. M. Mitchell, N. Butchart, M. P. Baldwin, and L. J. Gray, 2015: Stratospheric influence on tropospheric jet streams, storm tracks and surface weather. *Nat. Geosci.*, **8**, 433–440, https://doi.org/10.1038/ngeo2424.

Kuroda, Y., and K. Kodera, 2001: Variability of the polar night jet in the Northern and Southern Hemispheres. *J. Geophys. Res.*, **106**, 20 703–20 713, https://doi.org/10.1029/2001JD900226.

Kushner, P. J., and L. M. Polvani, 2004: Stratosphere–troposphere coupling in a relatively simple AGCM: The role of eddies. *J. Climate*, **17**, 629–639, https://doi.org/10.1175/1520-0442(2004)017<0629:SCIARS>2.0.CO;2.

Leith, C. E., 1975: Climate response and fluctuation dissipation. *J. Atmos. Sci.*, **32**, 2022–2026, https://doi.org/10.1175/1520-0469(1975)032<2022:CRAFD>2.0.CO;2.

Limpasuvan, V., D. W. Thompson, and D. L. Hartmann, 2004: The life cycle of the Northern Hemisphere sudden stratospheric warmings. *J. Climate*, **17**, 2584–2596, https://doi.org/10.1175/1520-0442(2004)017<2584:TLCOTN>2.0.CO;2.

Lorenz, D. J., and E. T. DeWeaver, 2007: Tropopause height and zonal wind response to global warming in the IPCC scenario integrations. *J. Geophys. Res.*, **112**, D10119, https://doi.org/10.1029/2006JD008087.

Martineau, P., S.-W. Son, M. Taguchi, and A. H. Butler, 2018: A comparison of the momentum budget in reanalysis datasets during sudden stratospheric warming events. *Atmos. Chem. Phys.*, **18**, 7169–7187, https://doi.org/10.5194/acp-18-7169-2018.

Matsuno, T., 1970: Vertical propagation of stationary planetary waves in winter Northern Hemisphere. *J. Atmos. Sci.*, **27**, 871–883, https://doi.org/10.1175/1520-0469(1970)027<0871:VPOSPW>2.0.CO;2.

——, 1971: A dynamical model of the stratospheric sudden warming. *J. Atmos. Sci.*, **28**, 1479–1494, https://doi.org/10.1175/1520-0469(1971)028<1479:ADMOTS>2.0.CO;2.

Maycock, A. C., and P. Hitchcock, 2015: Do split and displacement sudden stratospheric warmings have different annular mode signatures? *Geophys. Res. Lett.*, **42**, 10 943–10 951, https://doi.org/10.1002/2015GL066754.

McInturff, R. M. E., 1978: Stratospheric warmings: Synoptic, dynamic and general-circulation aspects. NASA Reference Publ. NASA-RP-1017, 174 pp., http://ntrs.nasa.gov/archive/nasa/casi.ntrs.nasa.gov/19780010687.pdf.

Mlawer, E. J., S. J. Taubman, P. D. Brown, M. J. Iacono, and S. A. Clough, 1997: Radiative transfer for inhomogeneous atmospheres: RRTM, a validated correlated-k model for the longwave. *J. Geophys. Res.*, **102**, 16 663–16 682, https://doi.org/10.1029/97JD00237.

Nakagawa, K. I., and K. Yamazaki, 2006: What kind of stratospheric sudden warming propagates to the troposphere? *Geophys. Res. Lett.*, **33**, L04801, https://doi.org/10.1029/2005GL024784.

Perlwitz, J., and N. Harnik, 2003: Observational evidence of a stratospheric influence on the troposphere by planetary wave reflection. *J. Climate*, **16**, 3011–3026, https://doi.org/10.1175/1520-0442(2003)016<3011:OEOASI>2.0.CO;2.

Plumb, R. A., and K. Semeniuk, 2003: Downward migration of extratropical zonal wind anomalies. *J. Geophys. Res.*, **108**, 4223, https://doi.org/10.1029/2002JD002773.

Polvani, L. M., and P. Kushner, 2002: Tropospheric response to stratospheric perturbations in a relatively simple general circulation model. *Geophys. Res. Lett.*, **29**, 1114, https://doi.org/10.1029/2001GL014284.

——, and D. W. Waugh, 2004: Upward wave activity flux as a precursor to extreme stratospheric events and subsequent anomalous surface weather regimes. *J. Climate*, **17**, 3548–3554, https://doi.org/10.1175/1520-0442(2004)017<3548:UWAFAA>2.0.CO;2.

Robinson, W. A., 2000: A baroclinic mechanism for the eddy feedback on the zonal index. *J. Atmos. Sci.*, **57**, 415–422, https://doi.org/10.1175/1520-0469(2000)057<0415:ABMFTE>2.0.CO;2.

Scherhag, R., 1952: Die explosionsartigen stratosphärenerwärmungen des spätwinter 1951/1952 (the explosive warmings in the stratosphere of the late winter 1951/1952). *Ber. Dtsch. Wetterdienstes*, **38**, 51–63.

Shaw, T. A., J. Perlwitz, and N. Harnik, 2010: Downward wave coupling between the stratosphere and troposphere: The importance of meridional wave guiding and comparison with zonal–mean coupling. *J. Climate*, **23**, 6365–6381, https://doi.org/10.1175/2010JCLI3804.1.

Shepherd, T. G., and T. A. Shaw, 2004: The angular momentum constraint on climate sensitivity and downward influence in the middle atmosphere. *J. Atmos. Sci.*, **61**, 2899–2908, https://doi.org/10.1175/JAS-3295.1.

——, K. Semeniuk, and J. N. Koshyk, 1996: Sponge layer feedbacks in middle-atmosphere models. *J. Geophys. Res.*, **101**, 23 447–23 464, https://doi.org/10.1029/96JD01994.

Sheshadri, A., R. A. Plumb, and E. P. Gerber, 2017: Propagating annular modes: Empirical orthogonal functions, principal oscillation patterns, and time scales. *J. Atmos. Sci.*, **74**, 1345–1361, https://doi.org/10.1175/JAS-D-16-0291.1.

Sigmond, M., J. F. Scinocca, V. V. Kharin, and T. G. Shepherd, 2013: Enhanced seasonal forecast skill following stratospheric sudden warmings. *Nat. Geosci.*, **6**, 98–102, https://doi.org/10.1038/ngeo1698.

Simpson, I. R., M. Blackburn, and J. D. Haigh, 2009: The role of eddies in driving the tropospheric response to stratospheric heating perturbations. *J. Atmos. Sci.*, **66**, 1347–1365, https://doi.org/10.1175/2008JAS2758.1.

——, P. Hitchcock, T. G. Shepherd, and J. F. Scinocca, 2011: Stratospheric variability and tropospheric annular-mode timescales. *Geophys. Res. Lett.*, **38**, L20806, https://doi.org/10.1029/2011GL049304.

Smith, K. L., and R. K. Scott, 2016: The role of planetary waves in the tropospheric jet response to stratospheric cooling. *Geophys. Res. Lett.*, **43**, 2904–2911, https://doi.org/10.1002/2016GL067849.

Song, Y., and W. Robinson, 2004: Dynamical mechanisms for stratospheric influences on the troposphere. *J. Atmos. Sci.*, **61**, 1711–1725, https://doi.org/10.1175/1520-0469(2004)061<1711:DMFSIO>2.0.CO;2.

Taguchi, M., T. Yamaga, and S. Yoden, 2001: Internal variability of the troposphere–stratosphere coupled system simulated in a simple global circulation model. *J. Atmos. Sci.*, **58**, 3184–3203, https://doi.org/10.1175/1520-0469(2001)058<3184:IVOTTS>2.0.CO;2.

Thompson, D. W. J., and J. M. Wallace, 2000: Annular modes in the extratropical circulation. Part I: Month-to-month variability. *J. Climate*, **13**, 1000–1016, https://doi.org/10.1175/1520-0442(2000)013<1000:AMITEC>2.0.CO;2.

——, and S. Solomon, 2002: Interpretation of recent Southern Hemisphere climate change. *Science*, **296**, 895–899, https://doi.org/10.1126/science.1069270.

——, J. C. Furtado, and T. G. Shepherd, 2006: On the tropospheric response to anomalous stratospheric wave drag and radiative heating. *J. Atmos. Sci.*, **63**, 2616–2629, https://doi.org/10.1175/JAS3771.1.

White, I. P., C. G. Garfinkel, E. P. Gerber, M. Jucker, V. A. Aquila, and L. D. Oman, 2019: The downward influence of sudden stratospheric warmings: Association with tropospheric precursors. *J. Climate*, **32**, 85–108, https://doi.org/10.1175/JCLI-D-18-0053.1.

Williams, G. P., 2006: Circulation sensitivity to tropopause height. *J. Atmos. Sci.*, **63**, 1954–1961, https://doi.org/10.1175/JAS3762.1.